Surface, Interface, and Nanostructure Characterization with Photoelectron Diffraction and Photoelectron and X-ray Holography

C. S. Fadley[#*]
In collaboration with:
Y. Chen[*], R.E. Couch[#], H. Daimon[‡*], R. Denecke[#*], H. Galloway[*@], Z. Hussain[†], A.P. Kaduwela[#*], Y.J, Kim[*&], P.M. Len[#*], J. Liesegang[£], J. Menchero[@], J. Morais[#], J. Palomares[*], S.D. Ruebush[#*], S. Ryce[*], M. B. Salmeron[*], W. Schattke[§], S. Thevuthasan[#], E.D. Tober[#*], M.A. Van Hove[*], Z. Wang[#*], R.X. Ynzunza[#*], and J.J. Zaninovich[#]

[#]*Department of Physics, University of California-Davis, Davis, CA 95616*
[*]*Materials Sciences Division, Lawrence Berkeley National Laboratory, Berkeley, CA 94720*
[†]*Advanced Light Source, Lawrence Berkeley National Laboratory, Berkeley CA 94720*
[&]*Department of Chemistry, University of Hawaii, Honolulu, Hawaii 96822*
[‡]*Dept. of Materials Physics, Osaka University, Toyonaka, Osaka 560, Japan*
[@]*Department of Physics, University of California-Berkeley, Berkeley, CA 94720*
[§]*Institut für Theoretische Physik, Universität Kiel, D-24118 Kiel, Germany*
[£]*Dept. of Physics, Latrobe University, Bundoora 3083, Victoria, Australia*

(Received: Feb. 7, 1997 Accepted: man. 10, 1997)

Abstract

The current status of photoelectron diffraction studies of surfaces, interfaces, and other nanostructures is first briefly reviewed, and several recent developments and proposals for future areas of application are then discussed. The use of full-solid-angle diffraction data, together with simultaneous characterization by low energy electron diffraction and scanning tunneling microscopy, to the epitaxial growth of oxides and metals is considered. Several new avenues that are being opened up by third-generation synchrotron radiation sources are also discussed. These include site-resolved photoelectron diffraction from surface and interface atoms, the possibility of time-resolved measurements of surface reactions with chemical-state resolution, and circular dichroism in photoelectron angular distributions from both non-magnetic and magnetic systems. The addition of spin to the photoelectron diffraction measurement is also considered as a method for studying short-range magnetic order. This spin sensitivity can be achieved either through core-level multiplet splittings or by circular-polarized excitation of spin-orbit-split levels. The direct imaging of short-range atomic structure by both photoelectron holography and two distinct types of x-ray holography using fluorescence emission is also now possible. Although much more recent in first experimental demonstration, x-ray holography shows considerable promise as a new method for studying the atomic structure of various types of nanostructures. Photoelectron holography with spin resolution also may make it possible to study short-range magnetic order in a holographic fashion.

1. Introduction

1.1 Photoelectron Diffraction and Holography

The basic process involved in photoelectron diffraction is illustrated in Fig. 1. A photon excites an electron from a core level that is necessarily well localized in space, and the outgoing photoelectron wave is scattered from the atoms neighboring the emitter, producing an interference pattern. It is the interference of the unscattered component ϕ_0 with the scattered components ϕ_j, (where j = 1, 2, 3, ... and is summed over a suitably convergent cluster of atoms) that produces the final diffraction pattern. Some of the key physical parameters controlling this process are indicated in the figure. These parameters are: $\hat{\varepsilon}$ = the light polarization which influences the initial photoelectron excitation matrix element, $\vec{k}$ = the electron wave vector or momentum $\vec{p} = \hbar\vec{k}$, $f_j(\theta_j)$ = the electron-atom scattering factor for a given scattering angle of θ_j (describable in first order via plane-wave scattering but more accurately via spherical-wave scattering), Λ_e = the attenuation length controlling the exponential damping of the elastic photoelectron signal due to inelastic scattering, $\overline{U_j^2}$ = the mean-squared atomic vibrational amplitude involved in the damping of the diffraction pattern due to vibrational effects (as included most simply in a Debye-Waller factor), V_0 = the inner potential producing refraction of the photoelectron in crossing this surface potential barrier, and Ω_0 = the effective

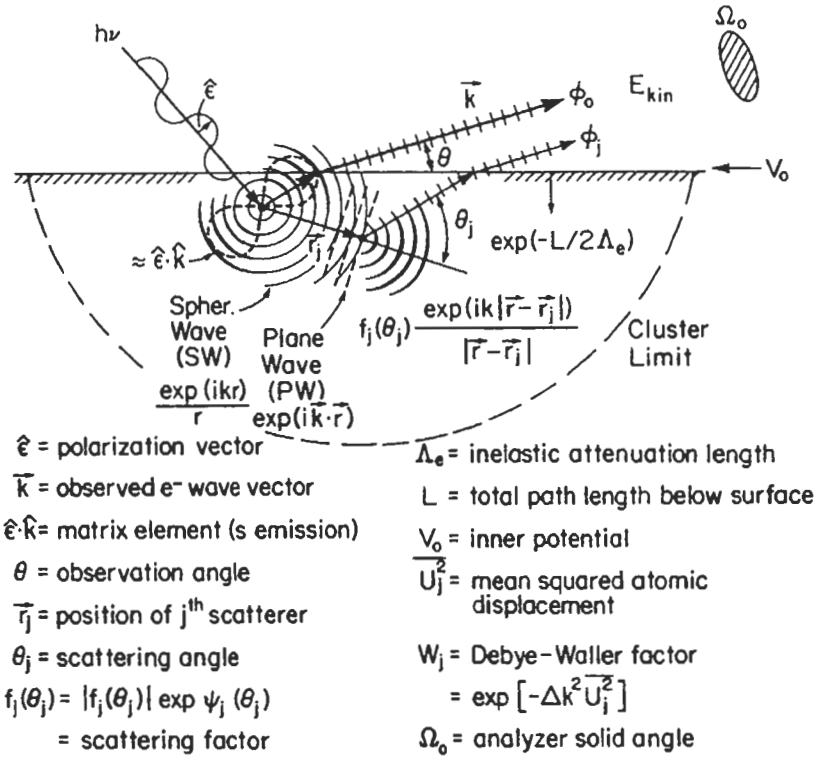

Fig. 1 Illustration of the basic photoelectron diffraction process, with various key physical quantities necessary for theoretically modeling such phenomena labelled and defined.

analyzer acceptance solid over which the diffraction pattern is averaged in the actual experiment. All of these aspects will be included in the theoretical calculations presented here.

Beginning with the first experiments and theoretical simulations of photoelectron diffraction [1], strong intensity modulations in intensity of as much as ±50% have been observed as a function of either the direction of electron emission or the energy of excitation, leading to what have been termed scanned-angle or scanned-energy measurements, respectively. The aim of these measurements is to deduce information about the atomic structure around a given type of emitter, or perhaps also the type of magnetic order surrounding such an emitter. There are by now a number of groups in the world engaged in such experiments, using both laboratory x-ray sources and synchrotron radiation (SR), and a variety of systems have been studied to date with this technique, including adsorbed atoms and molecules, systems exhibiting surface core-level shifts, epitaxial overlayers, surface structural and magnetic phase transitions, and atoms at buried interfaces. Several reviews of this field have appeared in recent years [2-7], and it will thus not be our aim to survey it in detail. Rather, we will begin by briefly describing those basic characteristics that make PD an attractive structural probe, consider some of its limitations and difficulties, and then go on to concentrate on several more recent developments involving both laboratory x-ray sources and next-generation SR sources that promise to make it an even more widely used tool for surface, interface, and nanostructure studies in the future.

We begin with the positive aspects of PD, several of which will be illustrated with more specific examples in the following sections:

1.1.1 Atom Specificity

PD is an atom-specific probe by virtue of the fact that a certain core level is probed. Thus, the structure around each type of atom in the sample can be probed separately.

1.1.2 Chemical-state or Site Specificity

With sufficient resolution, core binding energy shifts with chemical state (e.g., the different oxidation states of a given atom) or binding site (e.g, between the bulk and surface of a metal or

semiconductor) can be used to study the atomic structure around each type of atom separately [8].

1.1.3 Spin-specificity

Although not nearly as much explored, the diffraction patterns of photoelectrons of different spins can also be studied separately, yielding the promise of determining the local magnetic order around both magnetic atoms and non-magnetic atoms surrounded by magnetic atoms. Such spin sensitivity can be achieved by using the multiplet splittings inherent in the core spectra of various transition metals or rare-earth elements, by exciting spin-orbit-split core levels with circular-polarized radiation, or by some unavoidable combination of these two effects [2,9]. This leads to what has been termed spin polarized photoelectron diffraction (SPPD). [9].

1.1.4 Variation of Light Polarization

Beyond using circular light polarization to produce spin polarization, varying polarization from linear (LP) to left or right circular (LCP or RCP, respecively) and/or to unpolarized (UP) further permits selectively directing the outgoing photoelectron probe wave into different regions of the atomic structure surrounding the emitter, so that complementary structural information can be obtained for different relative orientations of light and sample [2,4].

1.1.5 Variation of Excitation Energy

PD makes use of the ability to vary the excitation energy (and thus also the photoelectron kinetic energy) in several ways. At higher kinetic energies of ≥500 eV, the magnitude of the electron-atom scattering factor $|f_j(\theta_j)|$ is highly peaked in the forward direction, producing pronounced peaks in diffraction patterns along e.g. bond directions in adsorbed molecules and low-index directions in epitaxial layers [2,3,5]. For lower energies of ≤300 eV, the scattering factor is more uniform over all directions, and often has a strong peak in the backward direction; thus, the locations of atoms behind the emitter as viewed from the detector can be studied [2,4,6], although their bond directions cannot be as directly determined as in forward scattering. Being able to vary energy between these two limits using synchrotron radiation thus permits studying the full structural environment of a given emitter. Going to lower energies in the 50-100 eV range further leads to increased sensitivity to the surface, as this is where most materials possess a minimum in the inelastic attenuation length Λ_e for electrons. Also, the 50-100 eV range is one in which magnetic scattering effects, particularly due to the exchange interaction are strongest; thus, such energies are those of relevance in SPPD measurements [9]. The energy dependence of the photoelectron de Broglie wavelength is of course also what leads to the modulations measured in scanned-energy photoelectron diffraction. And finally, being able to tune the photoelectron energy to maxima or minima in the various photoelectric cross sections is a useful possibility in SR studies.

1.1.6 Simple First-order Theoretical Interpretation

In a number of studies to date, it has proven possible to derive useful surface structural information by comparing experimental data to the results of rather straightforward single-scattering (SS or kinematical) theoretical calculations [2,3(a)]. However, it is also by now clear that a fully quantitative treatment of all of the features in both low-energy and high-energy diffraction patterns will require more sophisticated calculations at a fully-converged multiple scattering (MS) level, and several approaches have been applied to this [10]. These calculations have many similarities to those used in low energy electron diffraction (LEED) analyses . We will below illustrate both types of theoretical analysis.

1.1.7 Short-range Order Sensitivity

The nature of the photoelectron emission process (into an outgoing spherical wave which decays as 1/r) and the inelastic scattering process (with very short attenuation lengths) can be shown to make PD a probe of short-range atomic or magnetic structure, with primary sensitivity to the first 5 or so spheres of neighbors around a given emitting site, or within a sphere of maximum radius ~20Å [2,4]. This can be of advantage in studying nanostructures which do not exhibit long-range order over a surface. LEED by comparison is generally used to probe longer-range order over perhaps 50-100Å, although spot profile analysis can now be used to derive shorter-range information.

1.1.8 Direct Derivation of Structural Parameters and Photoelectron Holography

A final advantage is that there are several ways in which it is possible to directly derive structural parameters from PD data with a minimum recourse to theoretical modeling. We have already noted that *forward scattering peaks* directly give bond or low-index directions [2,3,5]. Beyond this, *Fourier transforms of scanned-energy PD data* yield path-length differences for different scatterers that can often be used to rule out some adsorbate geometries in a search for the true structure [2,4,6(b),11]. Finally, *holographic transforms of larger data sets* that involve varying both energy and angle over some volume in the momentum space or $\vec{k}$ space of the photoelectron can be used to directly derive atomic positions in three dimensions [12-20]. This was first suggested by Szöke [12(a)]. The process is illustrated in Fig. 2(b), in which the unscattered component ϕ_0 is now identified with the holographic reference wave and the scattered components ϕ_1, ϕ_2, ϕ_3, ... with the object or subject waves. Various methodologies for holographic inversions have recently been compared, and general criteria for optimizing the taking of such holographic data so as to minimize measuring times and realize the most accurate atomic images are also discussed [15(e)-(g)].

By contrast, some difficulties and limitations of PD are:

1.1.9 More Complex Instrumentation

Relative to a standard laboratory x-ray photoelectron spectroscopy (XPS) system, a more precise, computer-driven sample manipulator is required. However, adequate manipulators are now available from various commercial sources. If high angular resolution is desired, special electron optics or tube-array collimators may also be necessary [21]. For the most versatile and powerful experiments with variable energy and/or variable polarization, access to a synchrotron radiation beamline is also necessary.

1.1.10 Longer Measuring Times

Measuring hundreds or perhaps even a few thousand separate core spectra to produce a single angle or energy scan or a more complex scan over both angle and energy that can be used in a holographic sense [12-20] can be very time consuming, and may take between hours and days with most present systems. However, state-of-the-art laboratory XPS systems and next-generation synchrotron radiation beamlines, coupled with appropriately high-throughput spectrometers and detectors, promise to reduce these times to the minutes to hours range. Such instrumentation should also permit a broader range of dynamical studies on surfaces. We discuss below one such experimental system at the Advanced Light Source in Berkeley, and some time-resolved surface kinetics measurements that have been performed with it.

1.1.11 Macroscopic Domain Averaging

As presently carried out, PD data is taken from the full area illuminated by the radiation, which is typically of the order of $1mm^2$ to $10mm^2$. Thus, many domains are averaged over, and structural conclusions can be confused by the resulting overlap of diffraction patterns from different site types. Various kinds of photoelectron microscopy are currently being tested at different synchrotron radiation sources around the world, as reviewed recently elsewhere [22]. These developments may ultimately permit doing PD on areas as small as a few hundred Å in radius, thus focussing on a single domain or nanostructure on the surface. This last prospect is to be sure a tour de force experiment for third-generation (or even fourth-generation) synchrotron radiation sources, but realizing it would be exciting indeed, as a further--and final-- space dimension could then be accessed.

1.1.12 More Complex Multiple-scattering Theoretical Interpretation

We have already noted above that data can often be analyzed to a useful point within a single-scattering framework, but future studies will no doubt make more use of the more quantitative multiple-scattering model. However, a number of groups by now have multiple scattering programs operating [10], and these will no doubt become faster, more accurate, and more user friendly, as they have in the LEED community. We illustrate the need for this more accurate modeling in specific cases discussed below.

In what follows, we will present a few recent examples of PD data and its theoretical interpretation, and also consider the development of next-generation

instrumentation for such measurements These examples are chosen primarily from the work of our group, but we believe that they are illustrative of both some current forefronts of PD studies and some of the more exciting future directions in this field.

1.2 X-Ray Fluorescence Holography

We will also consider a much more newly developed technique for directly determining atomic structures, but one which is a very close relative of the previously-mentioned photoelectron holography (PH): x-ray holography (XH) [23,24]. In PH, the photoelectric effect creates an outgoing photoelectron wave from a given atomic center. As noted previously, the unscattered component of this wave is treated as a reference wave which interferes with the scattered components, with the latter being treated as the object or subject waves in a standard holographic exposure (cf. Fig. 2(b)). In the first method of doing XH, the deexcitation of a core hole in a given atom creates an outgoing fluorescent x-ray, with the unscattered and scattered components of this wave again serving as reference and subject in a holographic exposure. This also is shown in Fig. 2(b), and it has been termed x-ray flourescence holography (XFH), with a second method called multi-energy x-ray holography (MEXH) to be introduced later. Because x-rays scatter much more ideally from atoms than electrons (i.e., much more weakly and isotropically, and with negligible scattering phase shifts ψ_j), one expects either way of doing XH to yield more accurate holographic images than those from PH. However, the intensity modulations in an x-ray hologram are also expected to be much weaker (by a factor of $\sim 10^{-3}$–10^{-4}), so that such experiments will be inherently more difficult to perform. The much greater penetration depths of x-rays in matter also means that XH can be used to probe nanostructures quite far below a surface, with surface or interface specific studies being possible only if a certain atomic type is present only in the region to be studied. XH thus shares some of the advantages of PD/PH : atom specificity, variation of exciting light polarization, an even simpler kinematical theoretical interpretation, short-range order sensitivity, and direct derivation of three-dimensional atomic structures. And it also shares some of the disadvantages: complex instrumentation, even longer measuring times, and macroscopic domain averaging unless some form of lateral microscopic focusing can be developed in the future. Nonetheless, the exciting promise of XH as a complement to the well-developed x-ray diffraction (XRD) methods for studies of atomic structure (cf. Fig. 2(a)) has led to a few pioneering measurements of this type that we will briefly overview below.

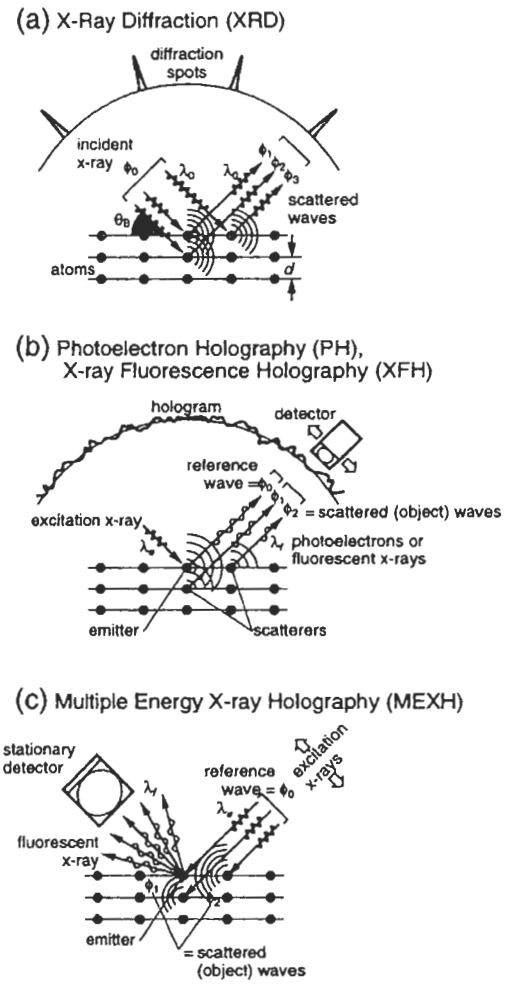

Fig. 2 Schematic illustration of some methods for determining atomic structure. (a) Conventional x-ray diffraction from a crystal, in which the incident wavefront ϕ_0 does not usually contribute to the diffracted intensity spots . (b) Localized-source holography in which a certain atom emits either a core photoelectron, yielding photoelectron holography (PH) or a fluorescent x-ray, yielding x-ray fluorescence holography (XFH). (c) A second type of x-ray holography in which the incident x-ray scatters from near-nrighbor atoms to create an interference at a certain emitter of fluorescent x-rays. This is the time-reversed version of XFH in (b).

2. Full-solid-angle Photoelectron Diffraction Data

Although the first full-solid-angle photoelectron diffraction pattern was measured some time ago [25(a)], it is only in recent years that these time-consuming experiments have been performed on a more routine basis, beginning particularly in the Osterwalder group [7, 25(b),(c)]. We here illustrate the utility of this kind of data in two recent studies of epitaxial growth: iron oxide on Pt(111) [26] and Cu on Ru(0001) [27]. In the iron oxide work, another noteworthy element was added in that x-ray photoelectron diffraction (XPD) measurements in a laboratory-based system were combined with *in situ* characterization by both LEED and scanning tunneling microscopy (STM), such that the complementary nature of these surface structure probes could be exploited simultaneously [26(b)].

Some data for a 1 monolayer (ML) overlayer of FeO on Pt(111) are shown in Fig. 3, where a LEED pattern, STM image, and full-solid-angle XPD patterns from all three atoms present (Pt, Fe, and O) as excited by Al Kα radiation (1,487 eV) are compared for the same surface preparation. The LEED pattern shows the basic Pt(111) spots, but with a rosette of superstructure spots around each one indicative of some longer range order. This longer range order can in turn be directly imaged by STM [26(a)], and it consists of a hexagonal unit cell of approximately 26Å×26Å superimposed on the atomic-resolution hexagonal oxide unit cell of 3.1Å×3.1Å. Such combined LEED and STM data led Galloway et al. [26(a)] to propose a particular superstructure or lateral Moiré pattern consisting of a hexagonal-symmetry bilayer of FeO(111) composed of a layer of Fe atoms on top of (or possibly below), a layer of O atoms. But this model left several questions about this overlayer unanswered. Among these questions were: Which atomic layer is outermost, Fe or O? What is the interplanar distance between Fe and O? Is there a preferred relative orientation of the FeO bilayer in its growth with respect to the underlying Pt?

The XPD results in Fig. 3(c) serve to answer all three of these questions. The Pt 4f diffraction pattern is dominated by scattering in the substrate crystal, and so does not contain any easily-derivable information concerning the structure of the overlayer. It does however provide a direct internal reference in the data for the orientation of the overlayer, with the [11 $\bar{2}$] direction lying in the Pt(111) surface indicated on the figure. The Fe 2p diffraction pattern contains three strong peaks with some fine structure around them, immediately suggesting that there are forward scattering atoms between Fe and the detector. Thus, O immediately appears to be the outermost layer. Finally, the O 1s pattern is devoid of any significant diffraction features, further confirming that it is the outermost layer. The second question as to interlayer spacing is also easily answered by measuring the polar angle of 20° at which the Fe-O forward scattering peaks occur, and combining this with the lateral unit-cell dimensions of the FeO overlayer as derived from LEED and/or STM. Simple trigonometry then yields an interplanar distance of only 0.65Å that is much contracted from the 1.25Å between (111) planes in bulk FeO. This distance can be further checked by carrying out single-scattering diffraction calculations for this overlayer, with single-scattering being an excellent approximation for this situation in which there are no chains of forward scattering atoms [2]. Comparing such calculations with experiment via R-factors (as done also in LEED structural analyses) finally yields the most accurate interplanar distance of 0.68Å that is very close to the simple estimate based on the forward scattering direction. Theoretical calculations for both 0.68Å and 1.25Å interplanar spacings are compared to experiment in Fig. 4. The agreement between experiment and the calculation for 0.68Å is excellent, including even the weak diffraction features around the forward scattering peaks. For a 1.25Å spacing, agreement is poor, both as to the polar angle position of the forward scattering peaks and the weaker features. Finally, the fact that there are only three forward scattering peaks in the Fe diffraction pattern immediately implies that only one orientation of the hexagonal O overlayer with respect to the underlying Pt surface exists, even though two O overlayer orientations rotated by 180° with respect to one another are equally likely as far as the Fe layer is concerned. Thus, there is an O-Pt interaction through the Fe layer that is strong enough to select only one orientation of the O overlayer; in fact, this interaction must involve second-layer Pt atoms. Thus, XPD can be used to determine a final subtle aspect of the growth process that would be difficult to arrive at with other methods.

This is thus an illustrative example of both how

useful full-solid-angle diffraction patterns can be (see also refs. 7 and 25 for other examples, including a very recent application to C_{60} [25(c)]) and how important it is to have additional complementary structural probes in the same experimental chamber, with LEED and STM being two particularly useful ones.

A second example of epitaxy recently studied using data from these combined techniques is Cu/Ru(0001), a system that at one level exhibits classic Stranski-Krastanov growth, but which on closer examination with STM by Günther et al. [27(a)] and with subsequent theoretical analysis by Hamilton and Foiles [27(b)] shows four stages of growth from a pseudomorphic first layer through various types of lateral contraction until finally reaching Cu(111) islands with essentially bulk Cu structure. Ruebush, Couch et al. [27c)] have measured full-solid-angle XPD from both Cu and Ru for this system, and analyzed these results together with the STM images obtained by Günther et al. [27(a)]. Some of their experimental data for 1, 2, 3 and 4 ML Cu coverages are shown in Fig. 5 together with theoretical calculations based upon both single-scattering cluster (SSC) and multiple-scattering cluster (MSC) methods. In general, MSC theory better describes these data, for example, as to the sharpness of the two sets of sixfold rings seen for 1 ML, and the relative intensities of the most intense forward scattering peaks for 4 ML. However, as noted before [2], SSC theory still predicts most of the major features. Comparing these XPD data with theory via R-factors has furthermore permitted determining the average interlayer spacing of the Cu overlayers as a function of overlayer thickness,

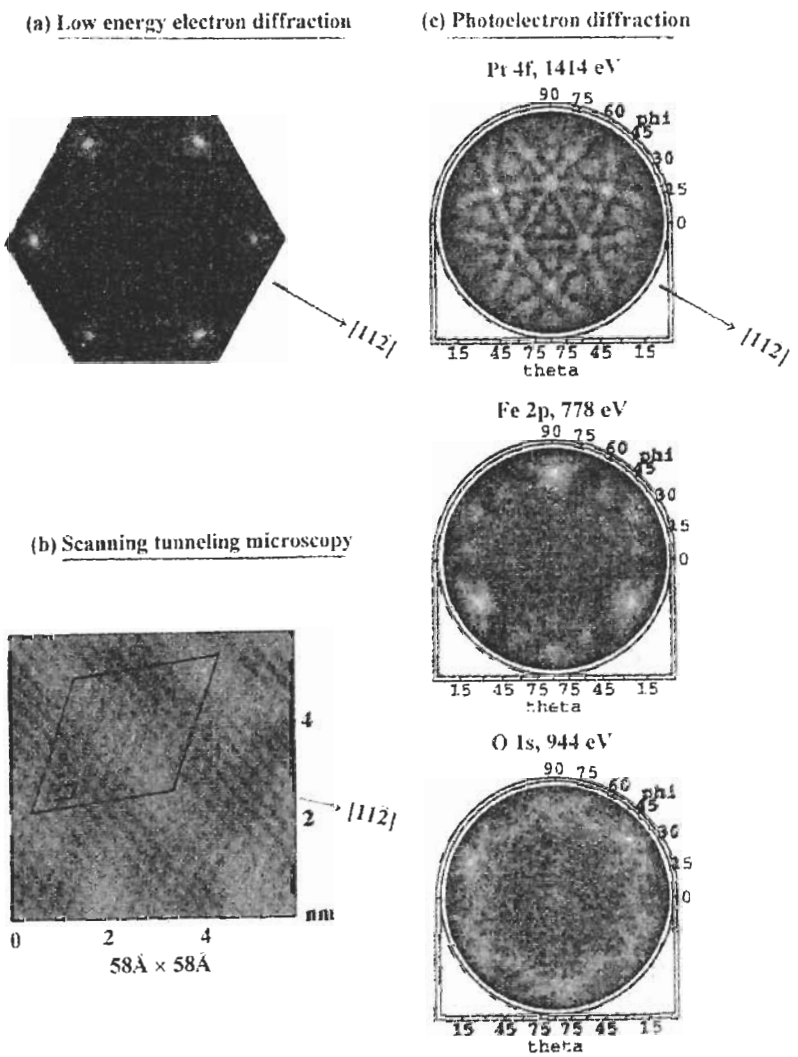

Fig. 3 LEED, STM, and XPD data for 1 monolayer (ML) of FeO on Pt(111). The full-solid-angle XPD patterns for Pt 4f, Fe 2p, and O 1s emission are shown. [From ref. 26(b).]

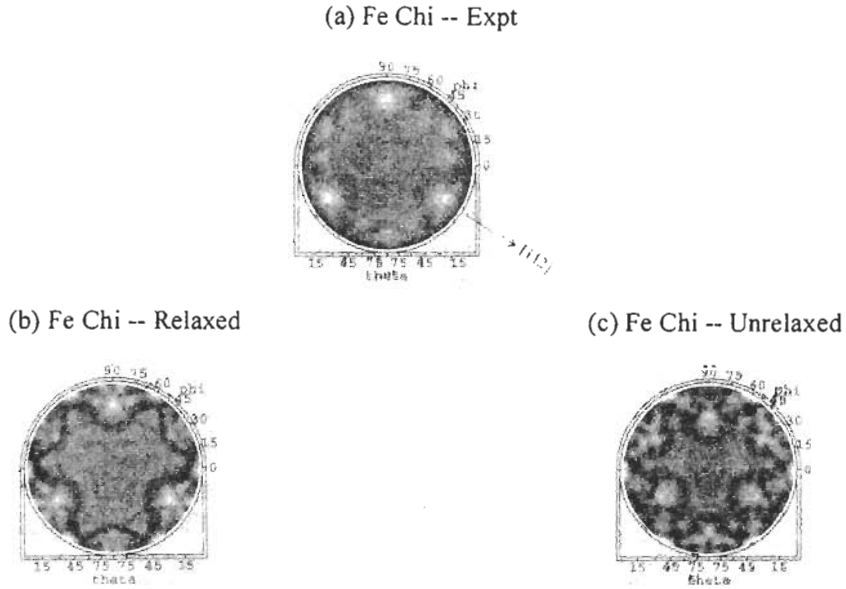

Fig. 4 The full-solid-angle Fe 2p XPD pattern for 1 ML of FeO on Pt(111): (a) experimental data, (b) single scattering theory with an Fe-O interplanar distance of 0.68 Å, (c) single-scattering theory with an Fe-O interplanar distance of 1.25 Å as in bulk FeO. [From ref. 26(b).]

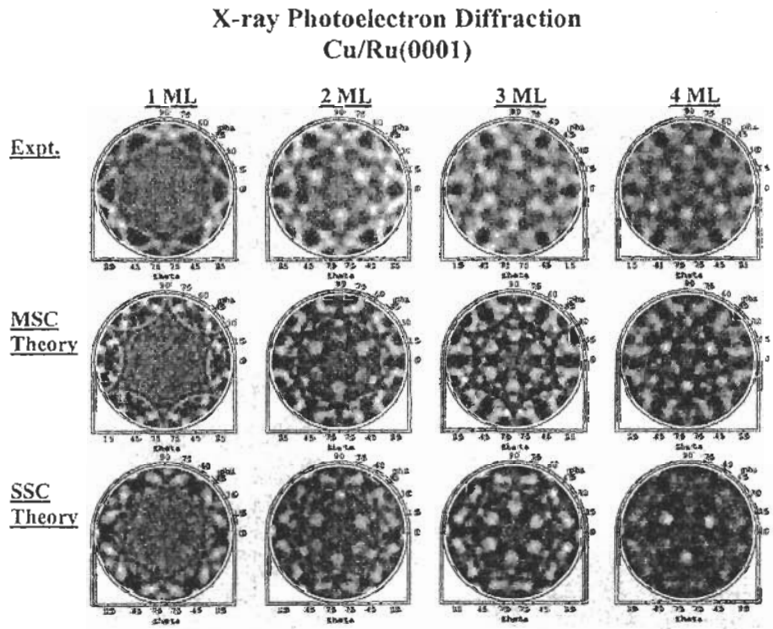

Fig. 5 X-ray photoelectron diffraction from Cu on Ru(0001), for coverages of Cu from 1 to 4 ML. Also shown are the results of multiple scattering cluster (MSC) and single scattering cluster (SSC) calculations. [From ref. 27(c).]

with the interesting result that significant contraction is found to persist even up to 5-8 ML coverages. A simple theoretical picture based on the Frenkel-Kontorova model [27(b)] on the other hand predicts a much quicker convergence to the bulk interlayer spacing than is seen in experiment [27(c)]. Accurately knowing such interlayer spacings is clearly important for an understanding of both the chemical reactivity and magnetic properties of such epitaxial metal overlayers, and full-solid-angle XPD can play a very useful role in such studies.

3. Photoelectron Diffraction Studies with Third Generation Synchrotron Radiation

There are at present several "third-generation" synchrotron radiation facilities either already operating or under construction, and these sources of very bright vacuum ultraviolet and soft x-ray radiation in roughly the 30-2000 eV range will permit a number of exciting new directions to be explored in both photoelectron diffraction and photoelectron holography. We illustrate some of these possibilities with data obtained by our group at the Advanced Light Source (ALS) in Berkeley, using a new high-resolution spectrometer/diffractometer that has recently been built for use there.

3.1 A NEXT-GENERATION PHOTOELECTRON SPECTROMETER/DIFFRACTOMETER

In Fig. 6, we show a schematic view of a photoelectron spectrometer that has been configured for high-resolution, high-intensity photoelectron spectroscopy, diffraction, and holography measurements, and installed on bending magnet Beamline 9.3.2 at the Advanced Light Source in Berkeley [2(f)]. Fig. 7 shows a photograph of the system, with major components labelled. The electron energy analyzer is a tuneable-resolution large-diameter hemispherical electrostatic system (Scienta ES200) that has been incorporated into a chamber which can rotate over 60 degrees in the plane of the electron storage ring. This rotation is made possible by a large-diameter bellows linking the chamber to the beamline, as shown in these figures. Such in-plane analyzer rotation, although common for much smaller analyzers mounted inside the vacuum system, has not been attempted before in such an *ex situ* mounting, and it permits selectively probing the fundamental photoelectron excitation cross section, keeping the photon-sample geometry fixed while measuring intensities over a large fraction of the 2π solid angle above the surface, and keeping the photoelectron-sample geometry fixed by scanning the analyzer synchronously with the sample polar-angle motion while measuring intensities as a function of light incidence direction. This analyzer is presently equipped with a single multichannel detector capable of an integrated count rate of about 100 kHz, but it will in the near future be modified so as to include a much higher speed multichannel detector operating up to the GHz

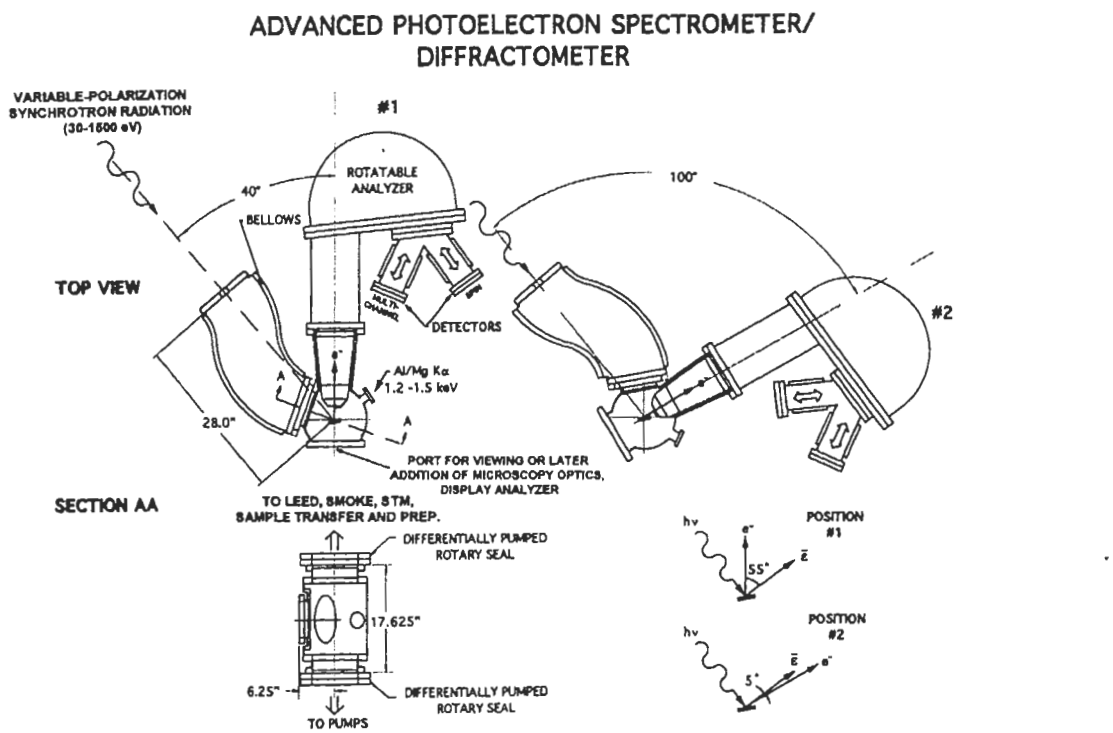

Fig. 6 Schematic drawing of the advanced photoelectron spectrometer/diffractometer (APSD) presently situated on beamline 9.3.2 of the Advanced Light Source. The rotation of the main chamber, including electron analyzer, and the range of photon-electron geometries possible are also indicated.

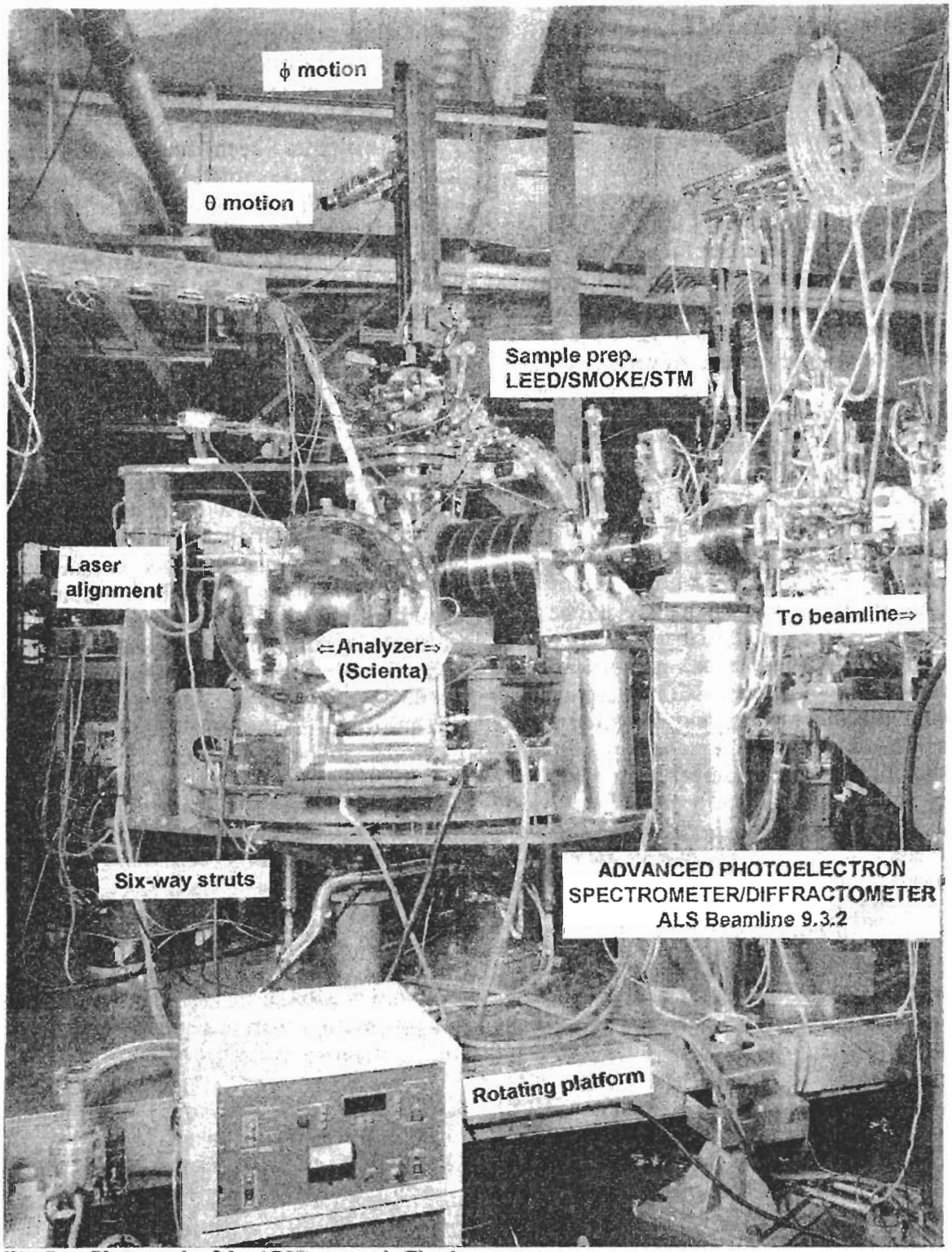

Fig. 7 Photograph of the APSD system in Fig. 6.

range, as well as an alternative spin detector of the so-called microMott type that will be interchangeable *in situ*. The spherical grating monochromator in this beamline, together with the Scienta analyzer , are capable of operating at overall kinetic energy resolutions of $\Delta E/E_{kin} \approx 1:10^4$. The analyzer is also equipped with a demountable collimator at its entry to limit both the solid angle of acceptance to ±1.5° for high angular resolution studies and the area of the sample surface seen by the analyzer. The 9.3.2 Beamline optics also permit taking radiation both above and below the plane of the electron orbit, thus obtaining a high degree of left or right circular polarization, as well as linear polarization with in-plane operation. We

discuss below the use of this capability in measuring circular dichroism effects in photoelectron angular distributions (CDAD). We now briefly consider some first results obtained with this instrumentation.

3.2 Full-solid-angle Photoelectron Diffraction from Surface and Bulk Atoms of a Clean Surface

In Fig. 8(a), we show the geometry for an experiment in which the surface and bulk W 4f peaks from a clean W(110) surface have been measured with this system. It is well known that the clean (110) surface exhibits a surface component shifted to lower binding energy by 320 meV [8(a), 28], and this is cleanly resolved in the spectrum of Fig. 8(b). The 120 meV full width at half maximum (FWHM) for the bulk peak is slightly narrower than anything measured before [28(a)], and is essentially limited by the various sources of natural linewidth for this level. PD has been measured before for this case [28(b)], but this work involved only a few scans in azimuthal angle or in energy. The high rate of data acquisition possible with this new system (a spectrum like that in Fig. 8(b) can be obtained in 20 sec or less) has now permitted measuring essentially the full solid angle of data for both the bulk and surface peaks, as shown in Figs. 9(a) and 9(b), respectively [29]. The photoelectron energies here are also in the very surface sensitive 39-40 eV range. Thus, it will be possible in the future to obtain much more complete state-specific photoelectron diffraction information, and we discuss the holographic use of such data below. One immediate benefit of such data sets is the possibility of making more rigorous tests of the multiple scattering theory that is now being used by several groups to analyze PD data. In particular, multiple-scattering and single-scattering calculations have been carried out to simulate these diffraction patterns [29], using programs developed by Kaduwela et al. [10(e)] and by Wu, Chen et al. [10(g)] and based on the convenient Rehr-Albers approximation for treating multiple scattering [10(d)]. These calculations have been carried out for a range of interlayer spacings between the surface W layer and the second layer below, with R-factors once more being used to determine the best estimate of the structure. Experiment and theory for the optimized distance are compared in Figs. 9(a)-(d), and the resultant R-factor curve from the more structure sensitive analysis of the surface-atom data presented in Fig. 9(e). There is excellent agreement between experiment and theory for the surface-atom diffraction pattern and reasonable agreement for the more complex bulk case, which involves emitters in various layers below the surface. The overall conclusion based on the surface diffraction pattern is that the surface W layer relaxes outward from the bulk position by 0.10±0.05Å, corresponding to a very small change of 4.4% of the bulk interlayer spacing. These results furthermore agree in general with prior studies of this surface by PD and LEED [28 and refs. therein]. Corresponding SSC calculations based on the same input parameters show similar diffraction features, but are not found to describe the data as well as the MSC results shown in Fig. 9. Thus, MS effects will definitely need to be included for a quantitative description of such low-energy data.

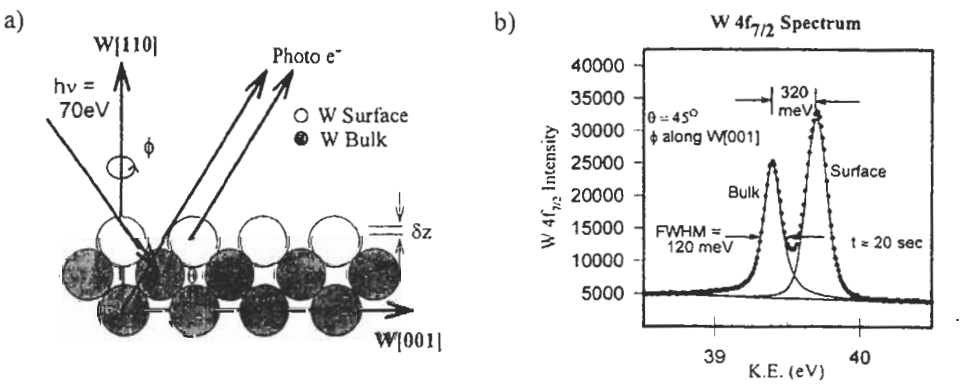

Fig. 8 (a) Schematic of the experimental geometry used to study clean W(110), showing the two types of W atom sites studied. (b) A high-resolution W $4f_{7/2}$ spectrum from W(110), showing the surface and bulk components. [From ref. 29.]

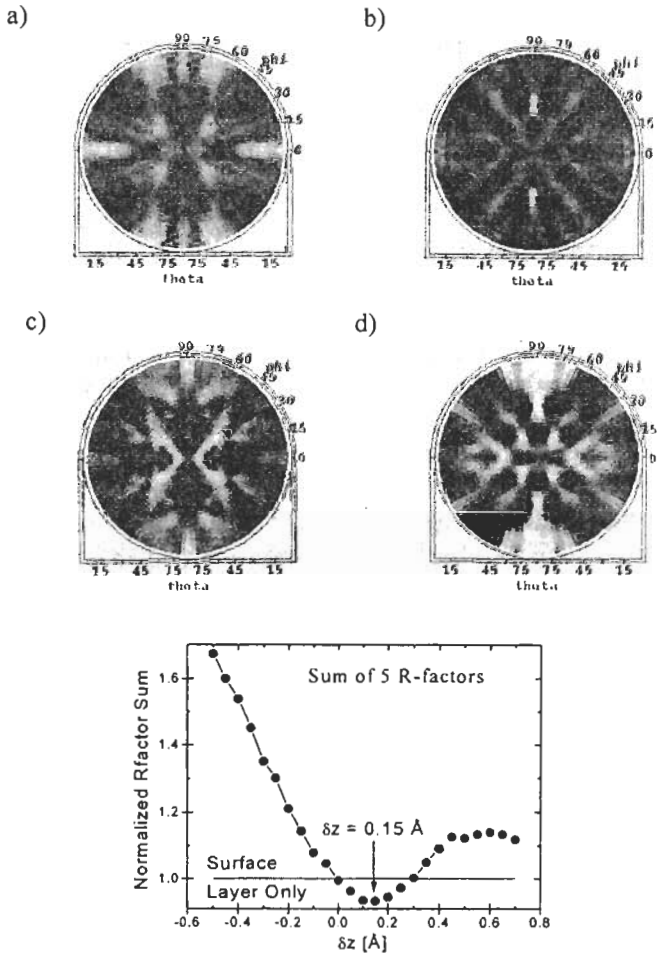

Fig. 9 Full-solid-angle W4f7/2 photoelectron diffraction patterns: (a) bulk-resolved experiment, (b) surface-resolved experiment, (c) bulk theory for the optimum interlayer distance, (d) surface theory for the optimum interlayer distance, and (e) R-factor comparison between experiment and multiple-scattering theory for the surface-atom W $4f_{7/2}$ photoelectron diffraction pattern of Fig. 9(b). The curve represents a normalized sum of five R-factors.. The horizontal line corresponds to an R-factor for calculations in which no bulk scatterers were present [From ref. 29.]

3.3 Photoelectron Diffraction From Interface Atoms

Determining the detailed structure of interfaces, e.g. between an epitaxial overlayer and the substrate on which it is grown, is clearly one of the most important current surface-structure problems. It is also a difficult problem to solve, because most surface structure probes either cannot uniquely resolve interface atoms from their neighbors or cannot probe very deeply below the surface. PD with high energy resolution has been shown capable of studying interface atoms that are at least a few atomic layers below the surface [8(b),(d),(e)], and future experimental capabilities promise to expand this application dramatically.

As one illustration of what is possible, we show in Fig. 10 photoelectron spectra obtained with the same experimental system at the ALS for the case of 1 ML of Fe and 1 ML of Gd deposited on W(110) [30]. The first monolayer of Fe is known to grow in a (1×1) structure on W(110), with presumably a single unique bonding site for every Fe atom [31]. On the other hand, it has been shown by Tober et al [32] in a combined STM and LEED study that the first monolayer of Gd forms a lateral superstructure or Moiré pattern with (7×14) periodicity in which a hexagonal Gd(0001) layer is formed on the surface with relatively little lattice constant change relative to bulk Gd. However, this layer is only weakly bound to the underlying W, and many types of Gd/W bonding sites are involved over the (7×14) unit cell. Fig. 10 compares W $4f_{7/2}$ photoelectron spectra from the clean surface in (a) with those from Fe/W in (b) and Gd/W in (c). The W

atoms at the Fe/W and Gd/W interfaces are clearly resolved from those in the bulk. For Fe/W, the second-layer W atoms are even displaced from the bulk due to their strong interaction with the Fe [31]. Thus, it has been possible to measure separate PD patterns for the
bulk and interface W atoms in these systems, and for Fe/W also for the second-layer W atoms, and to use these to directly probe the metal-metal interface structure [30]. Some of these data for Fe/W are shown in Fig. 11. Because there are many scattering geometries between either an interface W atom or a bulk W atom and the overlying Gd atoms, we find that the interface Gd/W diffraction patterns are very much like the clean-surface diffraction patterns, and that the two bulk curves are also very similar [30]. Thus, The Gd scattering here overall acts to simply produce a nearly uniform background of intensity underneath the dominant pattern associated with W-atom scattering. But for the Fe/Gd case, the interface-atom diffraction is much different from the

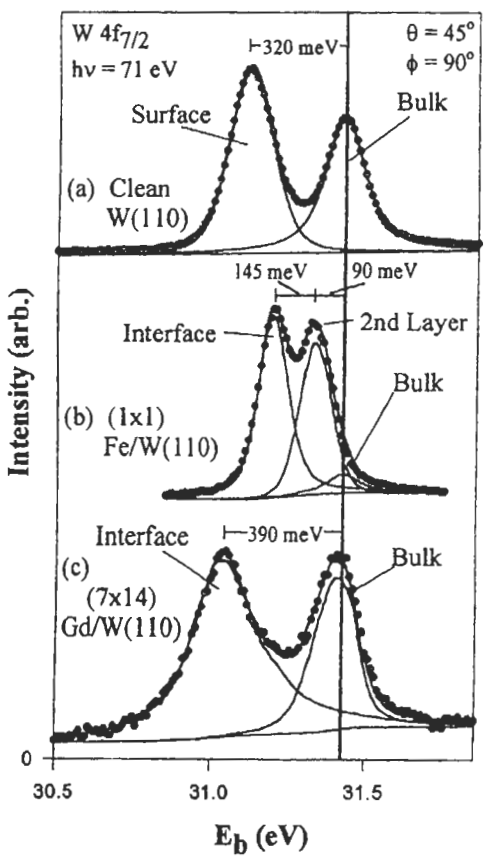

Fig. 10 W $4f_{7/2}$ photoelectron spectra taken with a photon energy of 71 eV from (a) the clean W(110) surface, (b) ~1 ML of Fe in a (1×1) overlayer on W(110), and (c) ~1 ML of Gd in a (7×14) Moiré superstructure on W(110). [From ref. 30.]

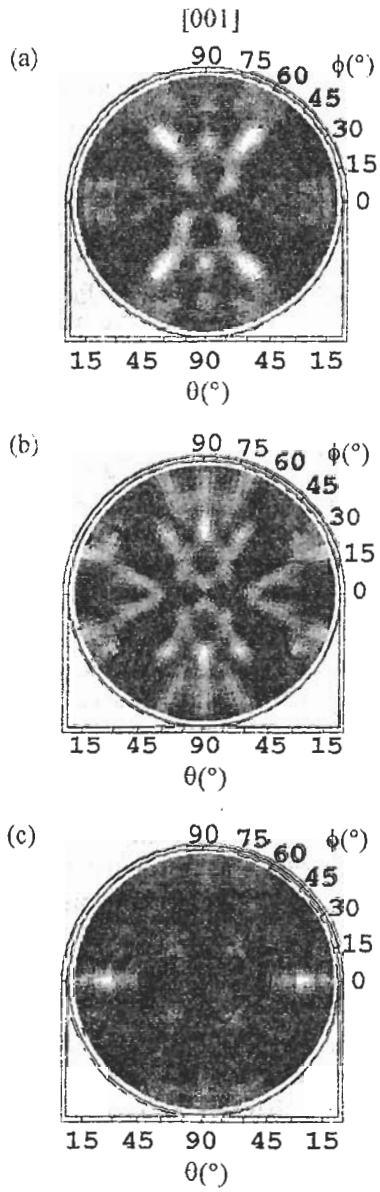

Fig. 11 Full-solid-angle W $4f_{7/2}$ photoelectron diffraction patterns for the (1×1) Fe/W(110) system taken from (a) experimental data for the –235 meV-shifted W interface peak, (b) theoretical multiple scattering calculations for the (1×1) Fe/W(110) interface with an optimized pseudo-threefold hollow adsorption site for the Fe, and (c) experimental data for the -90 meV-shifted W 2nd-layer peak. The photoelectron kinetic energy outside the surface was E_{kin} = ~40 eV in all cases. The data shown span takeoff angles relative to the surface from 12° to 90°(normal emission), and the W(100) azimuth is toward the top of the page in each of these stereographic projections. [From ref. 30.]

clean surface diffraction (compare Fig. 11(a) with Fig. 9(b)) . Thus, for this case, comparisons of experiment with theory for different Fe bonding geometries via R-factors has permitted determining the bonding site (a twofold bridge site which corresponds to continuing the W crystal) and the Fe-W interlayer distance (2.17 Å). Future applications of high-resolution interface PD to metal-metal, metal-semiconductor, and oxide semiconductor overlayer growth are therefore very promising.

3.4 Time-dependent Measurements

We now consider the possibility of time-resolved measurements of surface reaction kinetics and atomic structure. To illustrate this, an initially clean W(110) surface was exposed to a constant O_2 pressure of 3×10^{-9} torr (riding on a base pressure in the system of 2×10^{-10} torr) and its reaction with oxygen monitored over 70 min. by taking many photoelectron spectra in rapid succession. We show in Figs. 12(a)-(c) three W $4f_{7/2}$ spectra from W(110) that were taken at the beginning, middle, and end of this rapid accumulation of over 180 spectra. Each spectrum was obtained in only about 20 sec, and this provides some idea as to how rapidly it should be possible to accumulate PD data in parallel to such time-resolved spectra in the future. Four distinct states of W are seen in these spectra (as described below). The quantitative time evolution of these states is shown in Fig. 12(d), where intensities have been derived by fitting appropriate peak shapes to each spectrum of the series. The clean-surface peak decays to zero intensity over about the first 20 min. and comcomitant with this, the bulk peak actually grows in intensity over about the first 10 min. Simultaneously, a peak due to W atoms in interaction with chemisorbed oxygen begins to grow in at about 0.35 eV higher binding energy than the bulk peak, reaching its maximum intensity after about 30 min. Finally, a peak due to W atoms more strongly bound to oxygen in an incipient-oxide like state begins to grow in just as the chemisorbed species reaches its maximum intensity. These data thus clearly indicate a strong interrelationship of these states via the kinetic mechanisms that are operative for this oxidation reaction, and further analysis of these results in this context is now underway. However, these data already illustrate the considerable potential for future studies of nanostructure growth kinetics in which intensities are measured at several key energies or directions as a function of time, thus yielding also time-resolved PD. With further optimization of the bend-magnet beamline and end station on which these data were obtained, and/or making the same type of measurement on a more intense third-generation undulator beamline, we estimate that it should be possible to improve these data acquisition speeds by at least one order of magnitude, and probably two, so that individual spectra could be obtained in $\sim10^{-1}$–10^{-2} seconds.

4. Circular Dichroism in Photoelectron Diffraction

4.1 Non-magnetic Systems

Circular dichroism represents another aspect of photoelectron diffraction that can be explored with synchrotron radiation, and we here briefly discuss its essentials, with more detailed accounts appearing elsewhere [33-37]. Circular dichroism in photoelectron angular distributions (often termed CDAD) was first observed for emission from a core-level for the case of an adsorbed molecule on a surface (C 1s emission from CO/Pd(111)) by Schönhense and co-workers [33]. This dichroism, or difference between the intensities with left and right circular-polarized light (I^{RCP} and I^{LCP}, respectively), is most conveniently measured via a normalized asymmetry that is defined as: $A_{CDAD} = [I^{RCP}(\hat{k}) - I^{LCP}(\hat{k})] / [I^{RCP}(\hat{k}) + I^{LCP}(\hat{k})]$, where $\hat{k}$ is the direction of electron emission. Changes in this asymmetry with direction by as much as ±75% were observed for CO/Pd. These measurements thus made it clear that even a non-chiral molecule can exhibit circular dichroism when it is fixed to a surface, provided that a certain geometrical condition is satisfied between the molecular axis $\hat{n}$, the light incidence direction $\hat{q}$, and $\hat{k}$: in particular A_{CDAD} can be non-zero whenever these three vectors are not co-planar. Such data were first interpreted using quantum-chemical theoretical methods for the isolated adsorbate molecule [34(a)]. However, the chirality must be associated with the final-state photoelectron wave function, since the initial core state is spherically symmetric. This suggests using a photoelectron diffraction point of view to interpret such results, as has been done more recently [34(b)]. In this picture, all information on the chirality is carried in the geometry of the light incidence, the locations of all scatterers around the emitter, and the direction of electron

emission. This approach thus permits easily including contributions to the dichroism from atoms in the substrate. PD calculations were in fact found to correctly predict the effects seen for CO/Pd(111) [34(b)].

More generally, it has now been realized that the emission from *any* core level in a single crystal specimen can exhibit non-zero CDAD effects, provided that the plane containing $\hat{q}$ and $\hat{k}$ does not also coincide with a plane of mirror symmetry perpendicular to the surface [35,36]. In particular, intensity distribution measurements for Si 2s and 2p emission from a Si(001) surface in a geometry with the light incident along the normal have shown that there are not only very strong CDAD effects of as high as ~±20%, but that the observed diffraction patterns exhibit what can in first approximation be qualitatively described as peak "rotations" across mirror planes perpendicular to the surface. Daimon et al. [35] have discussed a simple physical model for understanding why individual features appear to rotate one way in azimuth with one polarization and the other way with the other polarization. This model considers the transfer of the z-component of angular momentum from the radiation to the outgoing photoelectron wave. In addition, more quantitative multiple scattering PD calculations have been shown to well predict these alterations in diffraction patterns with a change in polarization [36].

More recent data obtained at the ALS confirm the generality of such peak rotations, but also more quantitatively show that additional peak distortions beyond a simple rotation can occur in changing from LCP to RCP [37]. The case studied was a 1 ML coverage of oxygen on W(110) in the incipient oxide overlayer associated with the +730 meV peak in Fig. 12(c), and prepared in a manner described previously [38]. The experimental geometry was very similar to that of the Si(001) experiment, and is shown in Fig. 13(a). The W 4f spectra for this surface shown in Fig. 13(b) are clearly split into oxide and bulk components, with a separation between them of 0.73 eV. In the solid curves of Figs. 13(c),(d), we show single azimuthal scans of the oxide and bulk peaks for a takeoff angle θ with respect to the surface of 26.5°, and with excitation by linear-polarized (LP) light, as well as circular-polarized LCP and RCP light. With LP excitation, the correct mirror symmetry across the [001] azimuth at $\phi = 90°$ is seen to within statistical uncertainty in both oxide and

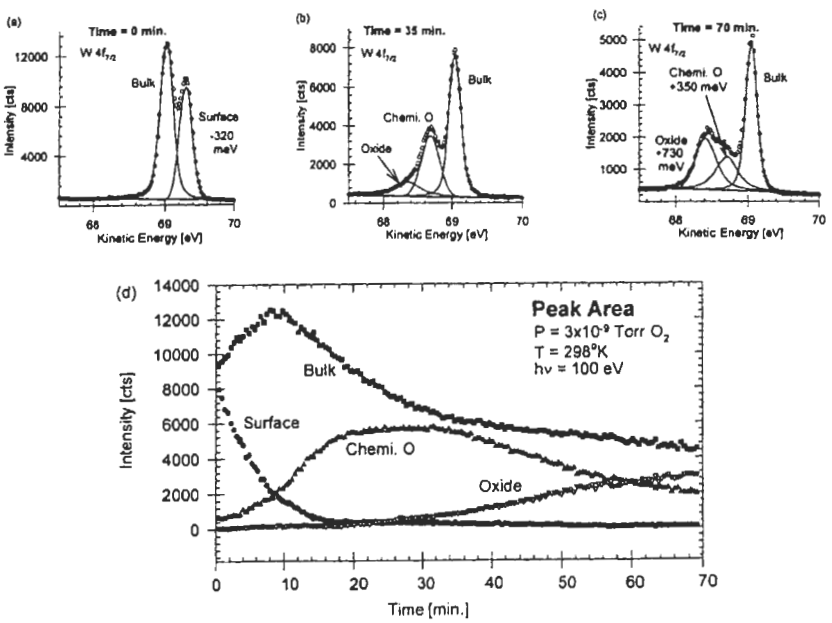

Fig. 12 Time and state resolved W $4f_{7/2}$ photoelectron spectra for a clean W(110) surface exposed to oxygen at 3×10^{-9} torr for 70 min.: (a) t = 0 min.--initial clean surface showing the surface core level shifted peak at –320 meV with respect to bulk; (b) t = 35 min--surface after 35 min., showing the two oxygen-induced peaks at –350 meV and –730 meV; (c) t = 70 min.--final spectrum of the series after 70 min, showing the increase of the oxide peak at the expense of the chemisorbed oxygen peak; (d) time dependence of the intensities of the four peaks observed in these spectra. [From ref. 29.]

bulk, but with LCP and RCP excitation, differences which can be interpreted as peak rotations, as well as other relative intensity changes and distortions, are found. The rotations appear as a general leftward movement of peaks and valleys with LCP, and a rightward movement with RCP. The overall diffraction patterns furthermore obey the symmetry expected from the normal-incidence experimental geometry, as the [001] mirror image of the LCP intensities for both oxide and bulk are within statistics identical to the RCP intensities. These symmetries and rotations are even more clearly seen in the large-solid-angle data sets in Fig. 14. In particular, a ±5° rotation of peaks is very clear in the oxide data between LCP and RCP. MSC PD calculations furthermore well predict both the overall rotations of features and the peak distortions seen here [37], with the dashed curves in Fig. 13(d) present some of these preliminary theoretical results.

Thus, such circular dichroism in photoelectron angular distributions is expected to be a very

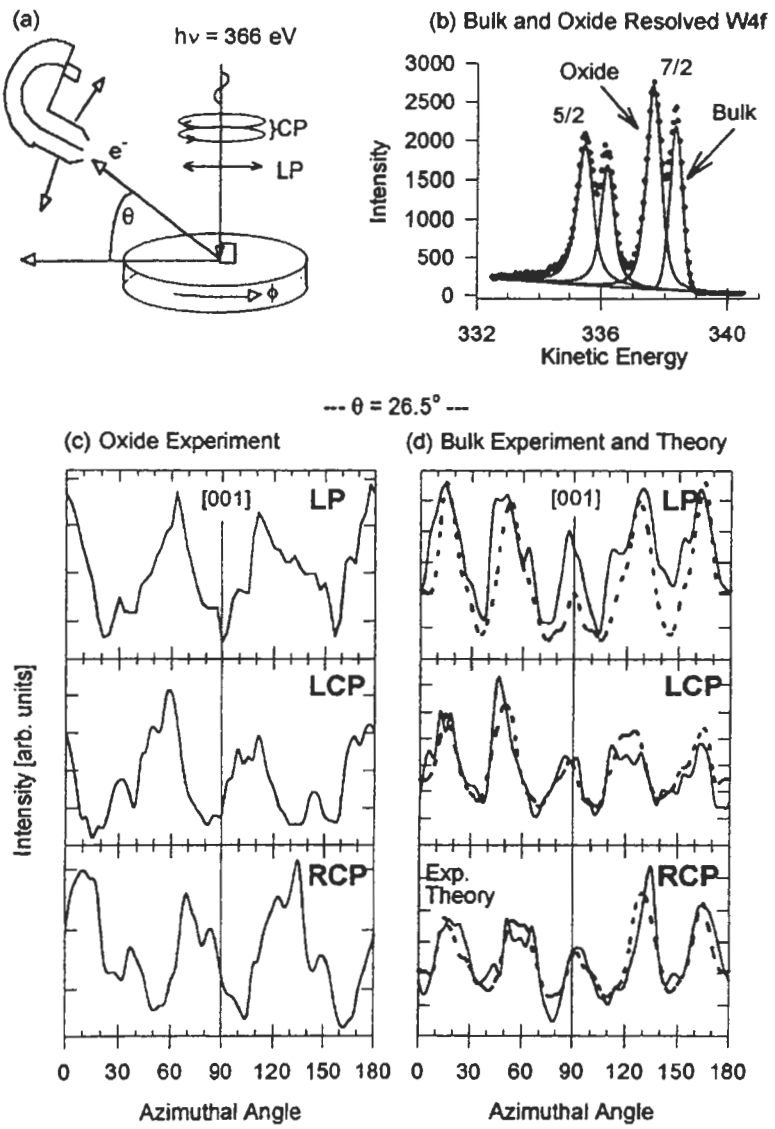

Fig. 13 Circular dichroism in the angular distributions of photoelectrons from (1×1)O/W(110) with a (1×12) oxide superstructure: (a) the experimental geometry, with radiation incident normal to the surface and the rotating analyzer of Figs. 6 and 7 being used to measure at various takeoff angles θ with respect to the surface; (b) a W 4f spectrum with oxide and bulk peaks resolved; (c),(d) azimuthal scans at a takeoff angle of 26.5° for both oxide and bulk W 4f components for linear-polarized (LP) light, left-circular-polarized (LCP) light, and right-circular-polarized (RCP) light. In (d) is also a comparison of the experimental curve for bulk emission with theoretical photoelectron diffraction calculations. [From ref. 37.]

general phenomenon for any non-magnetic system (or by implication, also any magnetic system), and such effects can also be quantitatively described by PD theory. One reason for being interested in this phenomenon is that circular dichroism in magnetic systems (*magnetic* circular dichroism or MCD) is often a much more subtle difference in intensities that may be only a few % in magnitude in 3d metals [39]. MCD effects in photoelectron angular distributions are due to a combination of the spin-orbit and multiplet splittings inherent in core spectra [39(a)], as well as possible spin-dependent exchange scattering from magnetic atoms during photoelectron escape from the surface [9]. By contrast, the CDAD effects discussed in this section are due to the strong Coulomb-plus-exchange scattering from every atom in the specimen. Thus, properly allowing for the latter will be essential to accurately measuring the former [34(b),35]. The same kind of allowance will be necessary in the more recently discovered magnetic linear dichroism (MLD) [40(a)] and magnetic unpolarized dichroism (MUD) [40(b)] effects in core photoelectron angular distributions.

4.2 Magnetic Systems

As a recent example of the kinds of *magnetic* circular dichroism effects seen in ferromagnetic systems, we show in Fig. 15(a) some recent Gd 4d spectra from Gd(0001) obtained by Morais, Denecke et al. [41]. Both of these spectra are split into various multiplets, with the five-

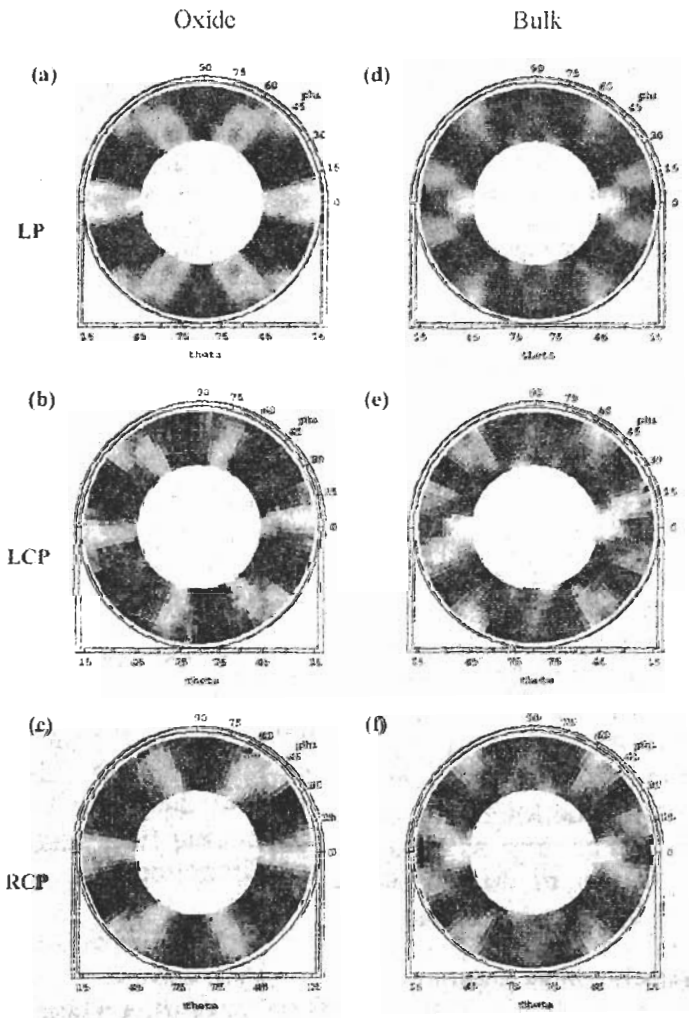

Fig. 14 Large-solid-angle photoelectron diffraction patterns for oxide [(a),(b),(c)] and bulk [(d),(e),(f)] W 4f emission from a (1×1)–(1×12) oxygen overlayer on W(110). Panels (a) and (d) are for LP excitation, (b) and (e) are for LCP excitation, and (c) and (f) are for RCP excitation. Note the apparent rotation of certain major features in the patterns between LCP and RCP, particularly for the oxide patterns. [From ref. 37.]

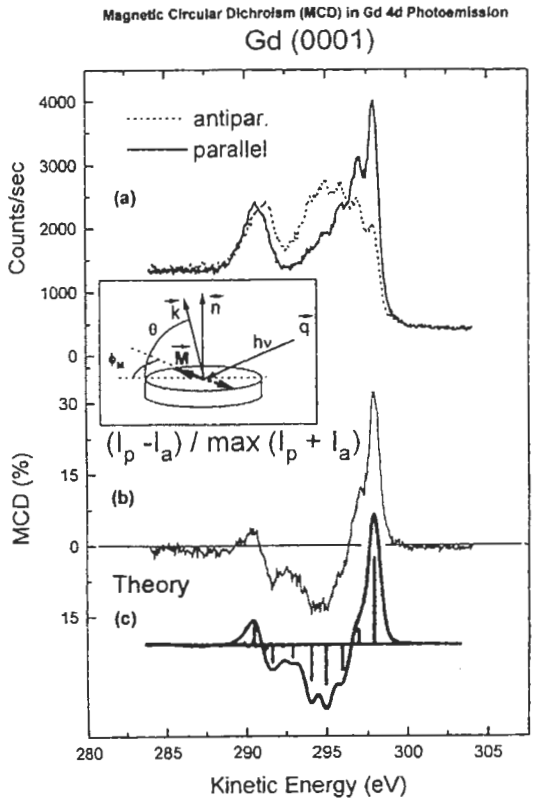

Fig. 15 Gd 4d photoemission spectra taken at a photon energy of 450 eV using left circular polarized light. The solid line spectrum was taken with the sample magnetization $\vec{M}$ parallel to the azimuth of the light indicence direction (Φ^{M}=0°), and the dotted line spectrum an antiparallel arrangement (ΦM = 180°). The lower curve is the normalized difference or MCD asymmetry. The inset shows the experimental geometry. [From ref. 41.]

component fine structure clearly resolved for the higher energy peak. The Gd has been magnetized in a mirror plane of the crystal, along $\vec{M}$ as shown in the inset, and the two spectra correspond to having $\vec{M}$ parallel or anti-parallel to the plane containing $\vec{q}$, the surface normal $\vec{n}$, and $\vec{k}$ (i.e., the angle ϕ_M = 0° or 180°). There is a dramatic difference between these spectra, and it results in the MCD signal shown in Fig. 15(b), which is as large as 30%. Fig. 15(c) now shows a free-atom theoretical calculation of such effects by Van der Lann et al. [42], and the agreement with experiment is excellent, including a state-by-state prediction of the degree of MCD.

Fig. 16 now shows the azimuthal angular dependence of this Gd MCD, with the sample being rotated about its normal so as to vary ϕ_M

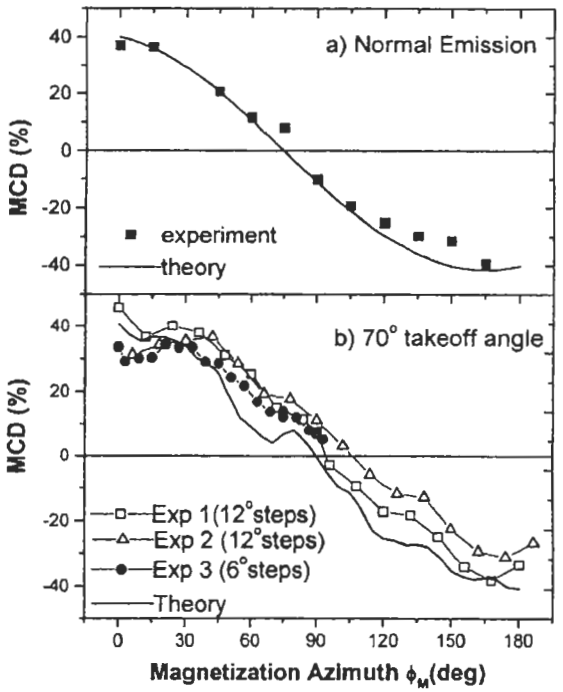

Fig. 16 Angle dependence of the overall MCD effect for Gd 4d core-level emission. (a) Normal emission, (b) Electron takeoff angle = 70° (20° from normal). In both cases the solid lines show theoretical curves calculated for the respective cases. In (a) the calculation is for a free atom, in (b) it is for emission from an atomic cluster three layers thick in order to account for photoelectron diffraction effects. [From ref. 41.]

and the MCD always being measured as a different of spectra for ϕ_M and ϕ_M + 180°. There is a strong ~±35% variation of this signal with ϕ_M, including an overall cosine-like behavior that is characteristic of the free atom and dominant in Fig. 16(a) for normal emission. But additional reproducible fine structure in the ~±5% range is also present in Fig. 16(b) for emission 20° off normal. Such MCDAD effects thus will be useful in studying magnetic order and local structure in an element-specific way, but it is clear that a fully quantitative understanding and use of them will require considering final state photoelectron scattering and diffraction.

5. Spin Polarization in Photoelectron Diffraction

5.1 Multiplet Splittings and Spin-polarized Photoelectron Diffraction:

Being able to separately measure intensity distributions for spin-up and spin-down photoelectrons should in principle make it possible to determine the short-range magnetic

order around a given type of emitter via what can be called spin-polarized photoelectron diffraction (SPPD). This is because the scattering of spin-up and spin-down photoelectrons is slightly different in the presence of magnetic order, primarily due to the exchange interaction between the photoelectron and the unfilled d or f valence shells responsible for the magnetic order. The use of multiplet splittings for deriving such spin-resolved spectra is by now well-established for both simple antiferromagnets [9] and ferromagnetic metals [43], and we show in Fig. 17(a) a multiplet-split 3s spectrum from antiferromagnetic $KMnF_3(100)$ that is one of the few cases studied to date by SPPD. The predominant spin polarizations of the two components are indicated in this figure, together with the overall electron configurations and L-S multiplets associated with each peak: the ^5S peak at lower kinetic energy is expected to be 100% up-spin and the ^7S peak 71% down-spin; *spin polarizations are in the case of such multiplets measured with respect to the emitting atom or ion.* The spin-up/spin-down intensity ratio in such multiplets has been measured previously for both $KMnF_3(110)$ and MnO(001) as a function of both temperature and direction [9(b)-(d)], and these results indicate some sort of high-temperature magnetic phase transition which occurs at 3-5 times the bulk transition temperature or Neél temperature. These experimental results are in qualitative agreement with PD calculations assuming that there is an abrupt loss of short-range antiferromagnetic order at these higher temperatures. One possible explanation for this effect is that there are local domains of short-range order that persist up to this higher temperature and then abruptly disappear. Another possibility discussed by Zhang et al. [44] is that the surface Néel temperature could be significantly higher than that in the bulk. Thus, it is also possible that these SPPD experiments have detected highly elevated surface Néel temperatures for these systems. Although further experiments and theoretical analysis will be necessary to fully clarify the nature of these observations, this work and other prior studies [9] indicates the potential of SPPD for the atom-specific study of short-range magnetic order. Exploiting this potential should be assisted enormously by the use of next-generation synchrotron radiation facilities.

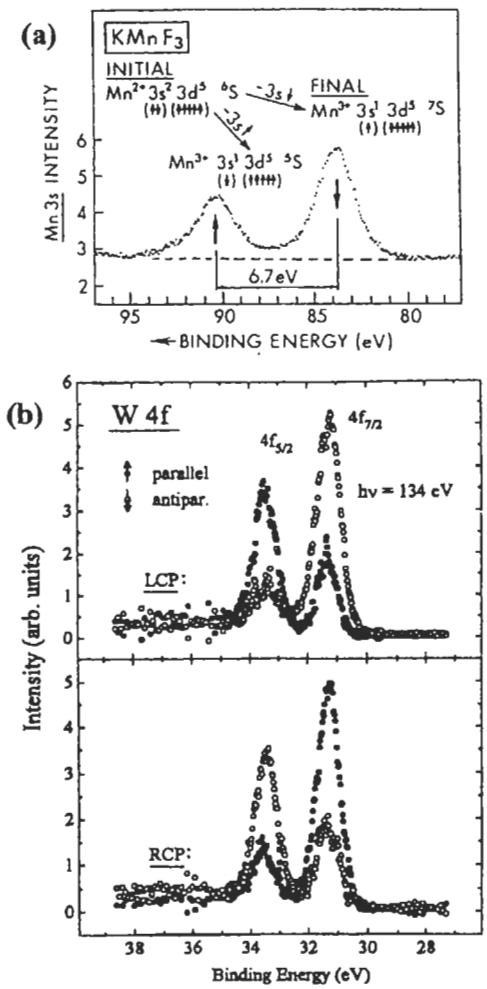

Fig. 17 Spin-polarized core photoelectron spectra: (a) a Mn 3s spectrum from $KMnF_3$, with the electronic states and spin polarizations relative to the emitting Mn^{2+} ion indicated [From ref. 9(e).]; (b) a spin-resolved W 4f spectrum from W(110), excited by LCP light (top panel) and by RCP light (bottom panel). In (b), the spin-resolved intensities as measured parallel or antiparallel to the light incidence direction q are indicated. [From ref. 46.]

5.2 Spin Polarization from Circular-polarized Excitation

Spin-polarized photoelectrons can also be produced by exciting a spin-orbit-split core level, making use of the well-known Fano effect from atomic physics [45]. We illustrate this with some very recent data obtained by Starke et al. for the non-magnetic system W(110) and shown in Fig. 17(b), using the experimental geometry shown in the inset between Figs. 18(b) and 18(c) [46]. Fig. 17(b) shows spin-resolved W 4f spectra for the two different circular polarizations of incident

radiation at an energy of 134 eV, with the photoelectron spin being measured either parallel or antiparallel to the resulting direction of the light helicity, which is in turn parallel or antiparallel to the light incidence direction. That is, for this case, the *spin polarizations are referenced externally to the direction of light incidence*. There is a clear and strong spin polarization in both the 5/2 and 7/2 components, with the expected change of sign as the polarization of the light is changed. These spin polarizations are also found to increase markedly with photon energy from 80 eV to about 130 eV, and to remain large at about 50-60% over the range from 130 eV to 240 eV, as shown in Fig. 18(a). These polarizations are thus comparable to the 70-100% expected for simple 3s multiplets of the type discussed previously for Mn, and immediately suggest using such spectra also as

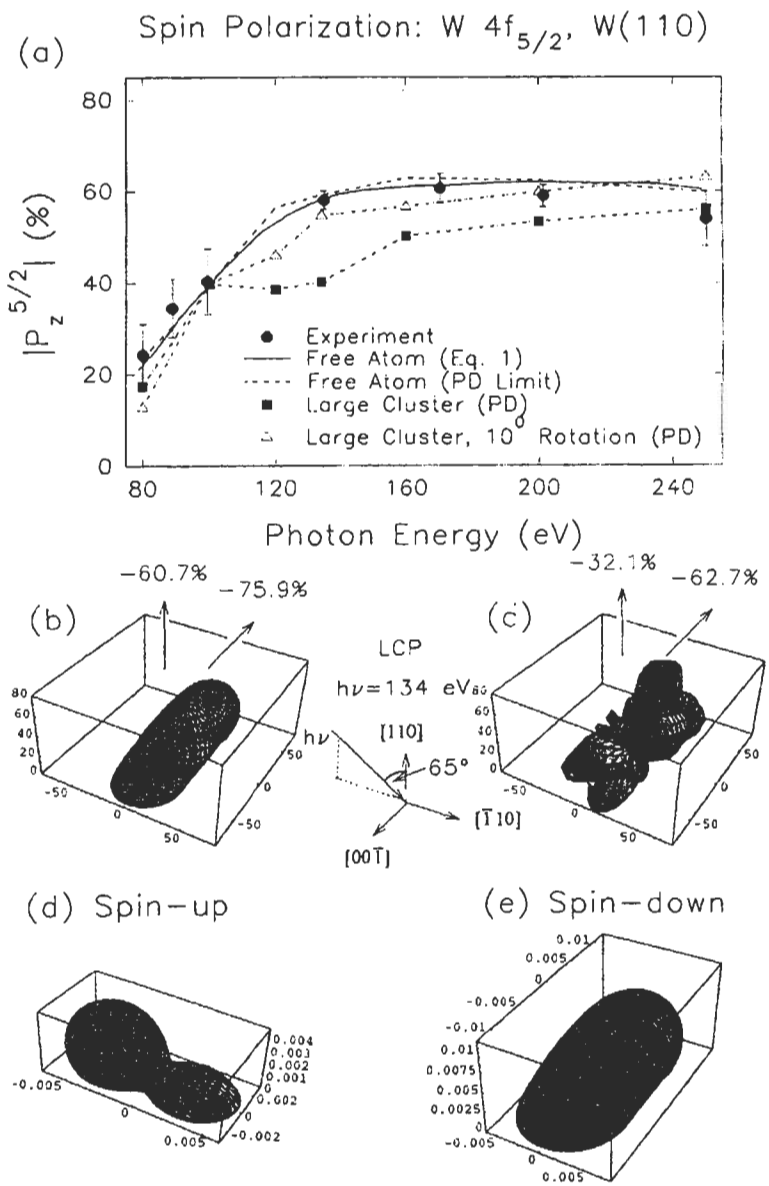

Fig. 18 Spin-polarization in W 4f spectra excited by circular-polarized light from W(110): (a) the absolute value of the $4f_{5/2}$ polarization as a function of photon energy, with experiment compared to both free-atom and MS cluster PD calculations; (b) the three-dimensional spin polarization for a free atom in the geometry shown in the inset and with an excitation energy of 134 eV; (c) as (b), but for a MS cluster PD calculation in a 5-atom cluster (an emitter below 4 surface scatterers); (d),(e) the separate spin-up and spin-down intensities excited in a free-atom. [From ref. 46.]

internal sources of spin-polarized photoelectrons for SPPD studies. Such SPPD studies based on circular-polarized excitation have in fact been attempted for the first time recently [47]. Theoretical calculations of such effects have also been carried out. For example, for the W $4f_{5/2}$ results in Fig. 18(a), simple free-atom calculations [48] agree very well with the energy dependence seen in experiment. MSC PD calculations from a large W(110) cluster in the nominal geometry of the experiment show the same general trend of polarization variation with energy as experiment, but have a significant dip at about 125 eV that is not observed experimentally. However, a small azimuthal rotation of the cluster by 10° that is within the experimental uncertainty of alignment suppresses this dip, and yields very good agreement with experiment as well. The change in the PD polarizations with cluster orientation however suggests that photoelectron scattering, *even in a non-magnetic lattice*, can significantly alter the degree of spin polarization in a core spectrum [46]. The origin of these changes is that the separate spin-up and spin-down intensity distributions excited from the 5/2 or 7/2 levels have very different shapes, and that they thus sample differently the non-magnetic scatterers around the emitting atom. These effects are illustrated in the theoretical calculations in Figs. 18(b)-(e): the three-dimensional distribution of polarization for the free-atom in (b) is significantly altered when emission from a 5-atom cluster is considered in (b) and this alteration can be qualitatively understood from the separate spin-up and spin-down intensity distributions for the free-atom in (d) and (e). Such effects should be very general, very strong, and occur in both non-magnetic and magnetic surroundings.

Finally, we note that the separate measurement of spin-up and spin-down intensities over a range of directions and/or energies can in principle lead to spin-polarized photoelectron *holography* [49], a prospect that we discuss briefly below.

6. Photoelectron Holography

We now turn to the potential for directly determining short-range atomic structures by holographically inverting data sets that may span both photoelectron direction and energy. All of these so-called "direct" methods involve carrying out some kind of mathematical operation that is closely akin to a fourier transform on a large set of data involving ≥1000 distinct intensity measurements. In general, the photoelectron intensity $I(\vec{k})$ for a certain wave vector $\vec{k}$ is converted to a normalized function $\chi(\vec{k})$ in a standard way via:

$$\chi(\vec{k}) = \frac{I(\vec{k}) - I_o(\vec{k})}{I_o(\vec{k})} \quad or \quad \frac{I(\vec{k}) - I_o(\vec{k})}{I_o(\vec{k})^{1/2}} \quad (1)$$

where $I_0(\vec{k}) \propto |\phi_0|^2$ is the intensity in the absence of any scatterers. Measurements of $\chi(\vec{k})$ are made at several directions of emission (several $\vec{k}$), and also perhaps at several energies of excitation (several $|\vec{k}|$). The most common way to holographically invert such a $\chi(\vec{k})$ data set is to carry out the following transform over the relevant volume in k-space, as first suggested by Szöke [12(a)], and amplified upon by Barton et al. [12(d)], and by Tong et al. [14(a)]:

$$U(\vec{r}) = \left| \int_{|\vec{k}|} \exp(-i|\vec{k}||\vec{r}|) \iint_{\hat{k}} \exp(i\vec{k}\cdot\vec{r}) \chi(\vec{k}) |\vec{k}|^2 \, d|\vec{k}| \sin\theta_k \, d\theta_k \, d\phi_k \right| \quad (2)$$

where θ_k and ϕ_k are the angles defining the direction k. Several prior studies have obtained successful three-dimensional images of near-neighbor atoms using this approach or close relatives of it [12-20], and it seems clear that, at least for back scattering atoms around a given emitter, very useful structural conclusions can be drawn. These images include some obtained with only one energy [e.g., 15(a),(b),(d); 17], and others in which the transform of Eq. 2 is modified to allow for non-ideal scattering effects and/or to somehow focus on the region of image space that is most nearly ideal [e.g., 13,14,15,18(b),(c),(d)].

We will illustrate this method as applied to a first-of-a-kind extended data set obtained by Rotenberg, Denlinger et al. [50] on Beamline 7.0 at the Advanced Light Source. The clean W(110) surface discussed previously has been used as a test case, with the intensities of the bulk and surface peaks in spectra such as that in Fig. 8(b) being measured over essentially the full hemisphere above the surface and for kinetic energies between 39 eV (like that in Figs. 8(b) and 9) and 309 eV. A total of about 20,000 unique intensities was thus measured. Fig. 19(a) now shows a holographic atomic image reconstructed via Eq. 2 (here referred to as Method A from among several considered

elsewhere [50]) from the surface-atom intensity data, as first normalized to produce $\chi(\vec{k})$ via Eq. 1. This image is in the vertical $(\bar{1}1\bar{2})$ plane, the emitter position is indicated by a dashed square, and the ideal positions of the neighboring atoms are indicated by circles. We see that the back scattering atom just below the emitter (denoted $[\bar{1}\bar{1}0]$) is very well imaged, with a sharp peak that is centered very close to the true atomic position (within ~0.2Å). The side scattering atoms surface atoms just next to the emitter (denoted $[\frac{\bar{1}\bar{1}\bar{1}}{222}]$ and $[\frac{\bar{1}11}{222}]$) are also clearly imaged, but with some smearing in the vertical direction, and positions that are further from the true positions, being shifted inward toward the emitter by about 0.7Å and downward from the surface plane by about 0.2Å. Nonetheless, this experimental image could be used to provide a good first-order estimate of the local geometry around these W surface atoms if it were not already known (e.g. via the PD analysis in Fig. 9).

In Figs. 19(b) and 19(c) are now shown corresponding images derived from both single scattering and multiple scattering calculations. Single scattering is found not to agree as well with experiment, for example for the form and relative intensity of the image of the back scattering atom. Multiple scattering is found to much better predict the image of this back scattering atom in both form and intensity. Both theoretical images are found to show a doubling of the side scattering atomic images that is not as evident in experiment, but they agree in predicting inward and downward shifts in the center of gravity of these images, as seen in experiment. Thus, experiment and multiple scattering theory are overall in very good agreement, but with the experimental images being even cleaner representations of these nearest-neighbor atomic images than found in theory.

Similar results for a bulk emitter are not as encouraging, with the forward scattering atoms above a typical emitter showing elongated and shifted images that would make it difficult to use them for a precise structural prediction [50]. Various other imaging algorithms have also been applied to these surface and bulk holographic data to assess the degree to which they improve the atomic images [50]. Overall, it is concluded that backscattering atoms below and side-scattering atoms beside a given emitter that is in turn at or near the surface can be imaged successfully, with forward scattering atoms above the emitter not being imaged as accurately. Large data sets of the type considered here should permit exploiting holographic imaging to a maximum degree in the future, although it should not be necessary for most cases to obtain more that 3,000-5,000 intensities to accurately image the near-neighbor region [15(e)-(f)].

We turn now to another intriguing prospect for the future of spin-resolved photoelectron diffraction studies: the possibility of directly imaging the scatterer spins around a given emitter via holographic inversion methods. We have already noted that two core photoelectron peaks can often be found at relatively close-lying energies that are strongly spin-polarized in an opposite sense. This might be due to a

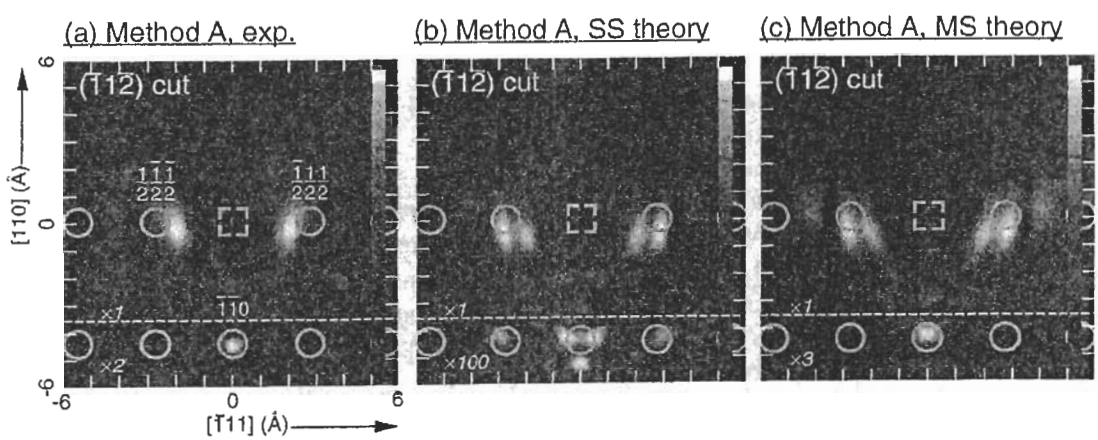

Fig. 19 W(110) holographic atomic images in the vertical $(\bar{1}1\bar{2})$ plane, as reconstructed from (a) a large experimental surface-resolved W $4f_{7/2}$ data set; and (b) corresponding multiple scattering calculations. The surface-atom emitter is indicated by a dashed square, and the near-neighbor scatterers by circles. Image intensities for vertical coordinates ≤–3.5 Å have been rescaled, with the scale factors indicated on the figures. [From ref. 50.]

core multiplet splitting or a spin-orbit doublet excited with circular polarization, or some mixture of these two effects. Thus, it is in principle possible to separately measure $\chi\uparrow(\vec{k})$ and $\chi\downarrow(\vec{k})$ for the two different spin orientations, and this could lead via spin-dependent scattering effects to the holographic imaging of the local magnetic order around a given type of emitter [49]. There are two obvious spin-sensitive imaging algorithms based on Eq. 2 and $\chi\uparrow(\vec{k})$ and $\chi\downarrow(\vec{k})$ [49(b),(c)]:

$$\Delta(\vec{r}) = U_{\uparrow}(\vec{r}) - U_{\downarrow}(\vec{r}) \qquad (3)$$

with obvious notation, and

$$\Delta'(\vec{r}) = \left| \int_{|\vec{k}|} \exp(-i|\vec{k}||\vec{r}|) \iint_{\hat{k}} \exp(i\vec{k}\cdot\vec{r}) \left[\chi_{\uparrow}(\vec{k}) - \chi_{\downarrow}(\vec{k}) \right] |\vec{k}|^2 \, d|\vec{k}| \sin\theta_k \, d\theta_k \, d\phi_k \right| \qquad (4)$$

which is just like the image $U(\vec{r})$ but calculated only on the difference of the spin-up and spin-down χ's. Additional vector-based spin-sensitive holographic imaging functions have also been proposed by Timmermans et al. [49(a)].

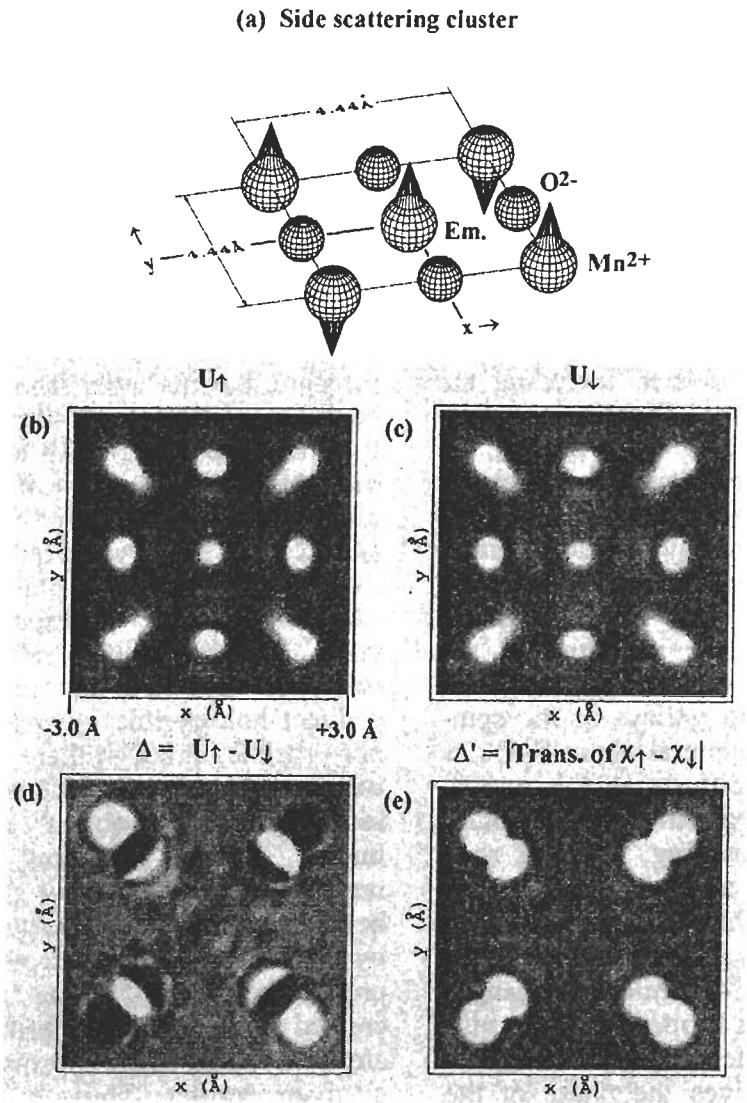

Fig. 20 A theoretical simulation of spin-polarized photoelectron holography: (a) a nine-atom cluster representing the (001) surface of MnO, with an emitter in its center; (b),(c) normal holographic images U(r) generated for the two different photoelectron spins by using Eq. 2 for holograms at 10 energies between 127 and 278 eV; (d) the spin-sensitive holographic image Δ generated by using Eq. 3; (e) the spin-sensitive holographic image Δ'(r) generated by using Eq. 4. [From refs. 49(c)(d).]

As a brief indication of the potential of this kind of photoelectron holography, we show in Fig. 20 holographic inversions of multiple scattering calculations for emission of spin-up and spin-down electrons from Mn^{2+} ions in a small planar cluster representing a portion of the MnO(001) surface [49(d)]. The cluster is shown in Fig. 20(a). Spin-up Mn^{2+} scatterers in this cluster have been distinguished from spin-down scatterers by having an additional exchange potential due to five unpaired 3d electrons that interacts only with spin-up photoelectrons. Spin-down scatterers have the same 3d exchange potential, but it interacts only with spin-down photoelectrons. Thus, the potential is slightly more attractive when the photoelectron spin is parallel to that of the scatterer. Spin-up and spin-down holograms were calculated in a fully-converged MSC way for 10 energies between 127 eV and 278 eV, and holographic images then derived via equations (2), (3), and (4). The normal images $U_\uparrow$ and $U_\downarrow$ in the plane of the cluster for spin-up and spin-down electrons are shown in Figs. 20(b),(c), together with the corresponding spin-sensitive images $\Delta(\vec{r})$ and $\Delta'(\vec{r})$ in Figs. 20(d),(e). The normal images show features for all of the atoms in the cluster, including the four non-magnetic O atoms. These spin-up and spin-down images are also very similar, as expected since the 3d exchange scattering is only 5-15% of the total effective scattering potential at these energies. By contrast, neither $\Delta(\vec{r})$ nor $\Delta'(\vec{r})$ contains any image intensity for the O atoms, verifying that either of these choices of imaging algorithm are predominantly sensitive to only the magnetic scatterers. The peaks and valleys in the spin-sensitive images are in general about 7-9% as strong in transform amplitude as the normal images, suggesting the experimental possibility of carrying out such imaging, albeit a non-trivial exercise. $\Delta(\vec{r})$ and $\Delta'(\vec{r})$ are also inherently different in that $\Delta'(\vec{r})$ images both orientations of scatterers in the same way, due the absolute value in Eq. 4, while $\Delta(\vec{r})$ changes sign when the scatterer is flipped, and thus also is sensitive to the orientation of a given scatterer. $\Delta(\vec{r})$ also involves the phase of the scattering factor, and thus can show sign changes over the region of a magnetic scatterer; however, it is clear from this and other calculations that the sign changes are exactly reversed if the orientation of the scatterer spin is flipped from up to down.

Thus, spin-polarized photoelectron holography represents an intriguing and challenging experimental possibility for the future, but one well matched to the new synchrotron radiation sources that are now becoming available.

7. X-ray Holography

We finally consider an alternative type of holography involving the scattering of x-rays by the near neighbors to a given atom that is emitting fluorescent x-rays. This method also was first suggested by Szöke [12(a)], and it has also been discussed previously from a theoretical point of view [23]. But the much weaker diffraction modulations involved have prevented the first experimental explorations of it until recently [24]. The first method for doing x-ray holography has been termed x-ray fluorescence holography (XFH) and is illustrated in Fig. 2(b). As indicated, it is identical in philosophy to photoelectron holography, except that it is now a fluorescent x-ray which scatters instead of a photoelectron. This makes the scattering much weaker, by 10^{-3} or 10^{-4}, but much more ideal and optical in character. The former means that such measurements will be more difficult to measure, but the latter means that they should be more accurate, and thus worth assessing. Comparing Fig. 2(a) with Fig. 2(b) also points out the fundamental difference between a classic x-ray diffraction (XRD) measurement and XFH. In XRD, scattered waves ϕ_1, ϕ_2, ϕ_3, ... from the various atomic planes in a sample *with long-range order* constructively interfere to yield various Bragg reflections, and the reference wave ϕ_0 is lost into the crystal. Thus, a direct holographic inversion of such data is not possible, although there are by now several well-established approaches for solving the resulting "phase problem" so as to determine unique atomic structures [51], and more recently, the use of x-ray standing waves has been discussed for this purpose [52(a)]. In XFH by contrast, the reference wave is involved in producing the diffraction pattern, which is created by the scattering from the near neighbor atoms involved in the *short-range order* around a given emitter. Thus, a true hologram is generated, and inversion of it using relationships like Eqs. 1 and 2 becomes feasible. Scattering of fluorescent x-rays from the long-range order in the crystal also can occur, and this produces features known as Kossel lines which have also been suggested as

an alternate way of doing x-ray holography [52(b)]. In fact, photoelectrons exhibit such features as well, which are called Kikuchi bands [53]. But we will focus here on the short-range-order effects in XFH that are completely analogous to a normal photoelectron diffraction pattern.

The first XFH measurements were performed recently by Tegze and Faigel [24(a)]. They measured the hologram by monitoring the single-energy Sr Kα emission (E = 14.10 keV, k = 7.145 Å) from a single crystal of $SrTiO_3$. Approximately 2,400 intensities were measured over a cone of 60° half angle above the surface. The final hologram was found to have anisotropies in intensity of $\Delta I/I_o \approx 0.3\%$. These much smaller effects mean that much more demanding detector counting statistics are required in x-ray holography measurements than with comparable electron holography measurements. The reconstruction of this hologram via the algorithm of Eq. 2 (as reduced to a single integral over direction) yields images of the Sr atoms only, as the much weaker scattering strength of the Ti and O atoms renders their images invisible compared to those of the Sr atoms. Fig. 21(a) shows the experimental image reconstructed in the vertical (010) plane (24(a)), and it is compared in Fig. 21(b) to an image reconstructed from a theoretical $\chi(\vec{k})$ for Sr Kα emission from a simple-cubic Sr cluster of 27 atoms (24(b)). The expected atomic image resolutions at this hologram energy and angular range are $\delta x \approx$ 0.3Å in the horizontal [100] direction, and $\delta x \approx$ 0.9Å in the vertical [001] direction [13(d)], and are in general agreement with the atomic images of Figs. 21(a),(b).

Reconstructing three-dimensional atomic images from a single-energy hologram yields twin images [12-15, 23]. In any structure without inversion symmetry, these twins can overlap with real atomic images so as to confuse structural interpretation. In addition, the real and twin atomic images for a particular energy and system can overlap completely out of phase, leading to an artificial suppression of atomic image intensities [23]. As in photoelectron holography, It is thus advantageous to reconstruct direct atomic images from multiple-wavenumber $\chi(\vec{k})$ data sets so as to avoid such real-twin image overlaps [12(c),12(d),23(c)]. However, such XFH holograms cannot be measured at arbitrary energies, with the latter being limited by the intensity and number of fluorescence lines of the photoemitting species.

To get around this single-energy or at most few-energy limitation in XFH, another method for obtaining x-ray holographic information at conveniently chosen multiple energies has also very recently been proposed and demonstrated experimentally for the first time by Gog et al. [24(c)]. This method has been termed multiple energy x-ray holography (MEXH), and its basic principle is illustrated in Fig. 2(c). MEXH is the time-reversed version of the conventional geometry of XFH (Fig. 2(b)), in that the wave motions are reversed, and the emitter and detector positions are interchanged. The

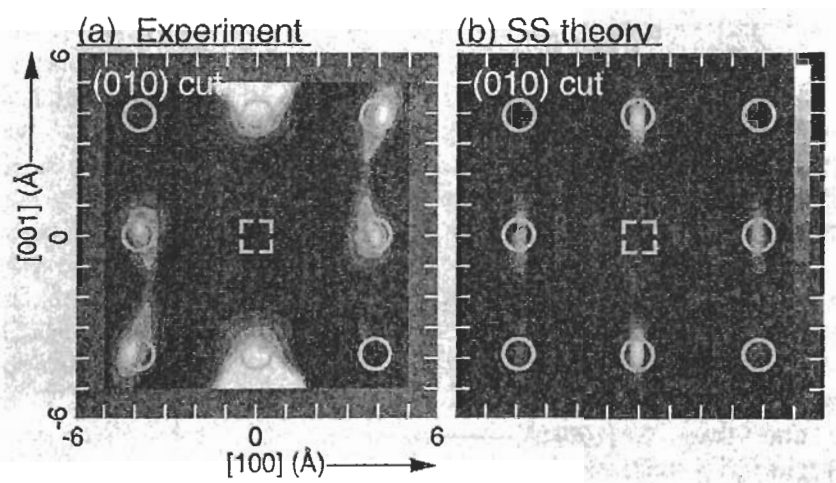

Fig. 21 X-ray fluorescence holography (XFH) atomic images of $SrTiO_3$ in the vertical (010) plane, obtained from (a) experimental [24(a)] and (b) theoretical [24(b)] Sr Kα $\chi(k)$ data sets, via Eq. 2. The Sr emitter site is indicated by the dashed square, and nearest-neighbor and next-nearest-neighbor Sr scatterers are indicated by circles.

exciting external x-ray beam now produces the reference and object waves, and the fluorescing atom acts only to detect the interference between the direct and scattered wavefronts. That is, the strength of the angle-integrated fluorescence signal is used to monitor the x-ray field strength at the emitting atom. The emitted x-rays are now collected by a distant detector with a large acceptance solid angle, in principle yielding much higher effective counting rates. The excitation x-ray source can also now be set to any energy above the fluorescence edge of the emitting species, thus permitting holograms at multiple energy and yielding in principle atomic images with no real-twin image overlaps [12(c),12(d),14(a),24(c)]. Specifically, multiple-energy x-ray holograms have been measured to date for hematite (α-Fe_2O_3(001))[24(c)], and for Ge(001) [24(d)].

We illustrate the results of applying the inversion algorithm of Eq. (2) to both experimental MEXH data for α-Fe_2O_3(001) measured by Gog and co-workers on Beamline X-14A of the National Synchrotron Light Source at Brookhaven National Laboratory [24(c)] and to theoretical simulations of this data. Fe Kα fluorescence was excited by horizontally polarized radiation at three energies in the range $h\nu$= 9.00keV to 10.30keV ($k = 4.561\text{Å}^{-1}$ to 5.220Å^{-1}) that was incident on the sample surface over a polar range of $60° \leq \theta \leq 90°$ = surface normal. These data points were measured at three energies with intervals of $\delta k = 0.329\text{Å}^{-1}$ (δE = 650eV), and at angular intervals of ($\delta\theta$, $\delta\phi$) = (5°, 5°), making a total of 435 unique measurements in a symmetry-reduced 1/3rd of the total solid-angle above the sample. The resulting modulation in $\chi(k)$ was ~0.5%, and thus comparable to that of the previously discussed XFH data.

For comparison to the experimental results, a single-scattering model [23(c)] was used to calculate a theoretical $\chi(k)$ for an ideal α-Fe_2O_3(001) cluster containing 384 Fe atoms with two inequivalent Fe emitter sites, as appropriate to the hematite lattice. The O atoms were not included due to their much smaller scattering power. The orientation of the radiation polarization with respect to the crystal during the crystal rotation of the measurement was also taken into account.. In particular, because the incident radiation is linearly polarized, the x-ray scattering factor must be further multiplied by the Thomson scattering factor, which has the form $\sin^2\Theta_e^{k'}$, where $\Theta_e^{k'}$ is the angle between the polarization vector of the incident radiation ε, and the direction k' of the scattered radiation. Thus, there will be nodes in the incoming scattered object waves along the polarization direction, and emitter atoms near this direction will not be strongly influenced by x-ray scattering.

Figs. 22(a) and (b) show the resulting atomic images for experiment and theory, respectively, in the [00$\bar{2}$] plane situated at z = –6.89Å below the emitter. There is excellent agreement between experiment and theory, and the positions of the atoms are very close to those in

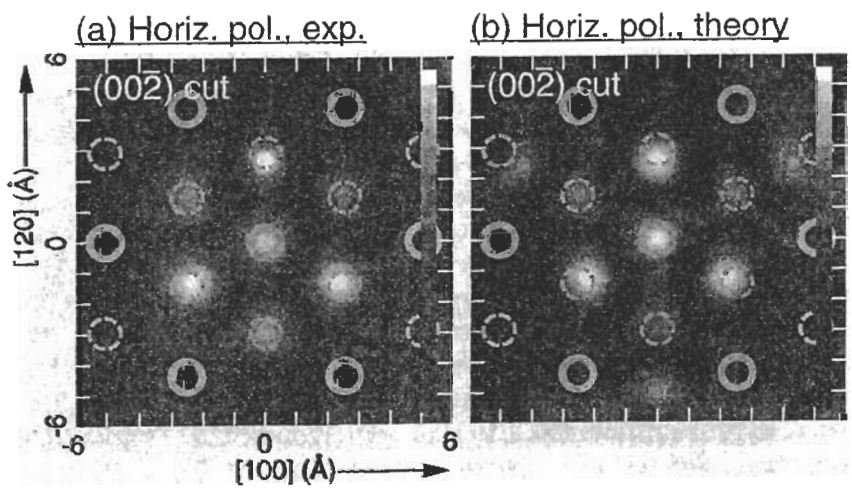

Fig. 22 Multiple energy x-ray holography (MEXH) atomic images of α-Fe_2O_3(001) in the horizontal (00$\bar{2}$) plane situated 6.89Å below each of the two types of Fe emitters, obtained from (a) experimental and (b) theoretical Fe Kα $\chi(k)$ data sets, via Eq. 2 [24(c)]. Fe scatterers in the bi-layer just above or below this plane are indicated by dashed circles, and Fe scatterers in relative positions common to both inequivalent Fe emitters are indicated by bold circles.

the known lattice (~0.2 Å inward displacement toward the emitter in experiment, and ~0.4 Å inward displacement in theory). The expected image resolutions in the horizontal ([100] and [1$\bar{2}$0]) directions are $\delta x=\delta y = 0.6$Å [13(d)] The experimental and theoretical images are very similar in that three of the Fe atoms from the neighboring upper bi-layer intrude into the [00$\bar{2}$] image plane. This intrusion is due to the limited energy and angular range of the $\chi(k)$ data points in k-space (as compared to the larger energy and angular range for the electron $\chi(k)$'s in the previous section), which results in atomic images much less resolved in the vertical [001] direction and a resolution limit of $\delta z \approx 2.5$ Å [13(d)]. Still, since these images are reconstructed from a multiple-energy $\chi(k)$ data set, they should be freer of real-twin image overlaps [23(c)]. And they show promise for future studies with data at more energies and over larger solid angle ranges.

Thus, although x-ray holography using fluorescent x-rays is really just beginning to become a reality, it already shows considerable promise of becoming a complementary tool to x-ray diffraction and other surface and bulk structure probes. Its key advantages are that it is element-specific, that the theoretical interpretation is much simpler than for electrons, and that it can probe the short-range structure in systems for which long-range order may be lacking. For certain kinds of surface, interface, and nanostructure work, both XFH and MEXH thus show considerable promise. Fully exploiting these new methods will also require the high brightness excitation sources of third-generation synchrotron radiation facilities.

8. Concluding Remarks

Photoelectron diffraction is thus in some respects a mature field, but at the same time one in which several exciting new possibilities for surface, interface, and nanostructure structure studies are found. The simple extension to taking full-solid-angle data often permits much clearer conclusions as to structures, especially when high energies with forward scattering are present, and complementary structure probes such as LEED and STM are used *in situ* with it. Next-generation instrumentation, particularly at third-generation synchrotron radiation sources, will much expand the use of chemical state- or site- resolved photoelectron diffraction, including the resolution of surface atoms and atoms at buried interfaces, time-dependent structural studies, and different types of dichroism in both non-magnetic and magnetic systems. The use of circular-polarized radiation for excitation shows up new phenomena in diffraction peak rotations and distortions, as well as making it possible to excite spin-polarized photoelectrons from any spin-orbit split level. Spin-polarized photoelectron diffraction and its more difficult cousin spin-polarized photoelectron holography also promise to provide information on local magnetic order in an element-specific, and also site-specific, way. Photoelectron holography also should provide direct imaging of short-range atomic structure, with useful accuracy for surface and near-surface species. Finally, x-ray holography of either the x-ray fluorescence type or the multi-energy time-reversed type represents a new and closely related technique with considerable potential for imaging short-range atomic structure with higher accuracy.

Acknowledgments

We are very grateful to various co-workers and collaborators who have contributed greatly to the beamline installation and testing, equipment fabrication, and some of the specific studies presented here: C. Cummings, T. Gog, K. Higashiyama, W.R.A. Huff, P.D. Johnson, S.A. Kellar, J. Kortright, T. Lauritzen, G. Materlik, C.E. Miner, E.J. Moler, M. Rice, D.A. Shirley, K. Starke, C. Westphal, R. Wright, H . Xiao, and F. Zhang. This work has been supported by the Director, Office of Energy Research, Office of Basic Energy Sciences, Division of Division of Materials Sciences, of the U.S. Department of Energy, under Contract DOE-AC03-76SF00098 and the U.S. Office of Naval Research under Contract No. N00014-94-0162.

References

1. (a) K. Siegbahn, U. Gelius, H. Siegbahn and E. Olsen, Phys. Lett. **32**A, 221 (1970); (b) C.S. Fadley and S.A.L. Bergstrom, Phys. Lett. **35**A, 375 (1971); (c) A. Liebsch, Phys. Rev. Lett. **32**, 1203 (1974); and Phys. Rev. B**13**, 544 (1976); (d) S. Kono, C.S. Fadley, N.F.T. Hall and Z. Hussain, Phys. Rev. Lett. **41**, 117 (1978); (e) D.P. Woodruff, D. Norman, B.W. Holland, N.V. Smith, H.H. Farrell, and M.M. Traum, Phys. Rev. Lett. **41**, 1130 (1978); (f) S.D. Kevan, D.H. Rosenblatt, D. Denley, B.-C. Lu, and D.A. Shirley,

Phys. Rev. Lett. **41**, 1565 (1978); (g) S. Kono, S.M. Goldberg, N.F.T. Hall, and C.S. Fadley, Phys. Rev. Lett. **41**, 1831 (1978); (h) M. Owari, M. Kudo, Y. Nihei, and H. Kamada, Japan. J. Appl. Phys. **19**, 1203 (1980).

2. (a) C.S. Fadley, Phys. Scripta T**17**, 39 (1987); (b) C.S. Fadley in *Synchrotron Radiation Research: Advances in Surface Science*, edited by R.Z. Bachrach (Plenum Press, New York, 1993); (c) C.S. Fadley, Surf. Sci. Repts. **19**, 231 (1993); (d) C.S. Fadley et al., J. Electron Spectrosc. **68**, 19 (1994); (e) C.S. Fadley, in *The Structure of Surfaces IV*, edited by X. Xide, S.Y. Tong, and M.A. Van Hove (World Scientific, 1994); (f) C.S. Fadley, M.A. Van Hove, Z. Hussain, and A.P. Kaduwela, J. Electron Spectrosc. **75**, 273 (1995).
3. (a) S.A. Chambers, Adv. in Phys. **40**, 357 (1990); S.A. Chambers, Surf. Sci. Rep. **16**, 261 (1992); (b) W.F. Egelhoff, Jr. in *Critical Reviews in Solid State and Materials Sciences*, **16**, 213 (1990).
4. (a) L.J. Terminello, X.S. Zhang, Z.Q. Huang, S. Kim, A.E. Schach von Wittenau, K.T. Leung, and D.A. Shirley, Phys. Rev. B **38**, 3879 (1988); (b) L.-Q. Wang, Z. Hussain, Z.Q. Huang, A.E. Schach von Wittenau, D.A. Shirley, and D.W. Lindle, Phys. Rev. B **44** , 13771 (1991); (c) D.A. Shirley et al., J. Electron Spectrosc. **68**, 49 (1994).
5. H.P. Bonzel, Prog. in Surf. Sci. **42**, 219 (1993).
6. (a) A.M. Bradshaw and D.P. Woodruff, in *Applications of Synchrotron Radiation: High-Resolution Studies of Molecules and Molecular Adsorbates on Surfaces*, edited by W. Eberhardt (Springer-Verlag, Berlin, 1993); (b) O. Schaff, G. Hess, V. Fernandez, K.-M. Schindler, A. Theobald, Ph. Hofmann, A.M. Bradshaw, V. Fritzsche, R. Davis. and D.P. Woodruff, J. Electron Spectrosc. **75**, 117 (1995).
7. J. Osterwalder, P. Aebi, R. Fasel, D. Naumovic, P. Schwaller, T. Treutz, L. Schlapbach, T. Abukawa, and S. Kono, Surf. Sci. **331-333**, 1002 (1995)
8. (a) D. Sebilleau, M.C. Desjonqueres, D. Chaveau, C. Guillot, J. Lecante, G. Treglia, and D. Spanjaard, Surf. Sci. Lett. **185**, L527, (1987); (b) C. Akita, T. Tomioka, M. Owari, A. Mizuike, and Y. Nihei, Jap. J. Appl. Phys. **29**, 2106 (1990); (c) A. Nilsson, H. Tillborg, and N. Mårtensson, Phys. Rev. Lett. **67**, 1015 (1991); (d) K.U. Weiss et al., Phys. Rev. Lett. **69**, 3196 (1992); (e) J.D. Denlinger, E. Rotenberg, U. Hessinger, M. Leskovar, and M.A. Olmstead, Appl. Phys. Lett. **62**, 2057 (1993), and E. Rotenberg, J.D. Denlinger, U. Hessinger, M. Leskovar, and M.A. Olmstead, J. Vac. Sci. Tech. B**11**, 1444 (1993).
9. (a) B. Sinkovic and C.S. Fadley, Phys. Rev. B**31**, 4665 (1985); (b) B. Sinkovic, B.D. Hermsmeier, and C.S. Fadley, Phys. Rev. Lett. **55**, 1227 (1985); (c) B.D. Hermsmeier, J. Osterwalder, D.J. Friedman, and C.S. Fadley, Phys. Rev. Lett. **62**, 478 (1989); (d) B.D. Hermsmeier, J. Osterwalder, D.J. Friedman, B. Sinkovic, T.T. Tran, and C.S. Fadley, Phys. Rev. B**42**, 11895 (1990); (e) B. Sinkovic, D.J. Friedman, and C.S. Fadley, J. Magn. Magn. Mater. **92**, 301 (1991).
10. (a) C.H. Li and S.Y. Tong, Phys. Rev. Lett. **42**, 901 (1979); (b) J.J. Barton and D.A. Shirley, Phys. Rev. B**32**, 1892 (1985); and Phys. Rev. B**32**, 1906 (1985); (c) A.P. Kaduwela, G.S. Herman, D.J. Friedman and C.S. Fadley, Phys. Scripta **41**, 948 (1990), as based on a method described in (d) J.J. Rehr and R.C. Albers, Phys. Rev. B41, 81139 (1990); (e) A.P. Kaduwela, D.J. Friedman, and C.S. Fadley, J. Electron Spectrosc. **57**, 223 (1991); (f) D.K. Saldin, G.R. Harp, and X.Chen, Phys. Rev. B**48**, 8234 (1993); (g) Y. Chen, H. Wu, and D.A. Shirley, private communication.
11. (a) P.J. Orders and C.S. Fadley, Phys. Rev. B**27**, 781 (1983); (b) M. Sagurton, E.L. Bullock, and C.S. Fadley, Phys. Rev. B**30**, 7332 (1984) and (c) Surf. Sci. **182**, 287 (1987)[24]; (d) V. Fritzsche and D.P. Woodruff, Phys. Rev. B**46**, 16128 (1992); and (e) P. Hofmann and K.M. Schindler, Phys. Rev. B**47**, 13942 (1993).
12. (a) A. *Szöke, in Short Wavelength Coherent Radiation: Generation and Applications*, edited by D.T. Attwood and J. Bokor, AIP Conference Proceedings No. 147 (AIP, New York, 1986); (b) J.J. Barton, Phys. Rev. Lett. **61**, 1356 (1988); (c) J.J. Barton, J. Electron Spectrosc. **51**, 37 (1990); (d) J.J.Barton,, and L.J. Terminello, paper presented at the Third

International Conference on the Structure of Surfaces, Milwaukee, July 1990, and in **Structure of Surfaces III**, S. Y. Tong, M. A. Van Hove, X. Xide, and K. Takanayagi, eds., (Springer Verlag, Berlin, 1991) p. 107, and J.J. Barton, Phys. Rev. Lett. **67**, 3106 (1991).

13. (a) G.R. Harp, D.K. Saldin, and B.P. Tonner, Phys. Rev. Lett. **65**, 1012 (1990); (b) G.R. Harp, D.K. Saldin, and B.P. Tonner, Phys. Rev. B**42**, 9199 (1990); (c) B.P. Tonner, Z.-L. Han, G.R. Harp, and D.K. Saldin, Phys. Rev. B**43**, 14423 (1991); (d) G.R. Harp, D.K. Saldin, X. Chen, Z.L. Han, and B.P. Tonner, J. Electron Spectrosc. **57**, 331 (1991); (e) D.K. Saldin, G.R. Harp, B.L. Chen and B.P. Tonner, Phys. Rev. B**44**, 2480 (1992); (f) D.K. Saldin, G.R. Harp, and B.P. Tonner, Phys. Rev. B**45**, 9629 (1992)
14. (a) S.Y. Tong, C.M. Wei, T.C. Zhao, H. Huang, and H. Li, Phys. Rev. Lett. **66**, 60 (1991); (b) S.Y. Tong, H. Li, and H. Huang, Phys. Rev. Lett. **67**, 3102 (1992); (c) S.Y. Tong, H. Huang, and C.M. Wei, Phys. Rev. B**46**, 2452 (1992); (d) J.G. Tobin, G.D. Waddill, H. Li, and S.Y. Tong, Phys. Rev. Lett. **70**, 4150 (1993).
15. (a) S. Thevuthasan, G.S. Herman, A.P. Kaduwela, R.S. Saiki, Y.J. Kim, W. Niemczura, M. Burger and C.S. Fadley, Phys. Rev. Lett. **67**, 469 (1991); (b) G.S. Herman, S. Thevuthasan, T.T. Tran, Y.J. Kim, and C.S. Fadley, Phys. Rev. Lett. **68**, 650 (1992); (c) S. Thevuthasan, G.S. Herman, A.P. Kaduwela, T.T. Tran, Y.J. Kim, R.S. Saiki, and C.S. Fadley, J. Vac. Sci. Technol. A**10**, 2261 (1992); (d) S. Thevuthasan, R.X. Ynzunza, E.D. Tober, C.S. Fadley, A.P. Kaduwela, and M.A. van Hove, Phy. Rev. Lett. **70**, 595 (1993); (e) P.M. Len, F.Zhang, S. Thevuthasan, A.P. Kaduwela, M.A. van Hove, and C.S. Fadley, J. Electron Spectrosc. **76**, 351 (1995); (f) P.M Len, S. Thevuthasan, A.P. Kaduwela, M.A. van Hove, and C.S. Fadley, Surf. Sci. **365**, 535 (1996); (g) P.M. Len, S. Thevuthasan, A. P. Kaduwela, C. S. Fadley, and M. A. Van Hove, J. Electron Spectrosc., to appear.
16. (a) L.J. Terminello, J.J. Barton, and D.A. Lapiano-Smith, J. Vac. Sci. Technol. B**10**, 2088 (1992) and Phys. Rev. Lett. **70**, 599 (1993); (b) B.L. Petersen, L.J. Terminello, and D.A. Shirley, Mat. Res. Soc. Symp. Proc. **307**, 285 (1993); (c) B.L. Petersen, L.J. Terminello, J.J. Barton, and D.A. Shirley, Chem. Phys. Lett. **220**, 46 (1994); (d) B.L. Petersen, Ph.D. Thesis, University of California-Berkeley, 1995; (e) L.J. Terminello, B.L. Petersen, and J.J. Barton, J. Electron Spectrosc. **75**, 299 (1995).
17. Y. Zhou, X. Chen, J.C. Campuzano, G. Jennings, H. Ding, and D.K. Saldin, Mat. Res. Soc. Symp. Proc. **307**, 279 (1993).
18. (a) H. Wu, G.J. Lapeyre, H. Huang, and S.Y. Tong, Phys. Rev. Lett. **71**, 251 (1993); (b) H. Wu and G.J. Lapeyre, Phys. Rev. B**51**, 14549 (1995); (c) S.Y. Tong, H. Li, and H. Huang, Phys. Rev. B**51**, 1850 (1995); (d) M.T. Sieger, J.M. Roesler, D.-S. Lin, T. Miller, and T.-C. Chiang, Phys. Rev Lett. **73**, 311 (1994).
19. M. Zharnikov, M. Weinelt, P. Zebisch, M. Stichler, H.-P. Steinrück, Surf. Sci. **334**, 114-134 (1995), and references therein.
20. R. Denecke, R. Eckstein, L. Ley, A.E. Bocquet, J.D. Riley, and R.C.G. Leckey, Surface Science **331-333**, 1085 (1995).
21. (a) M. Owari, M. Kudo, Y. Nihei, and H. Yamada, J. Electron Spectrosc. **22**, 131 (1981); (b) R. C. White, C.S. Fadley, and R. Trehan, J. Electron Spectrosc. **41**, 95 (1986)
22. B.P. Tonner, D. Duhham, T. Droubay. J. Kikuma, J. Denlinger, and E. Rotenberg, J. Electron Spectrosc. **75**, 309 (1995).
23. (a) M.Tegze and G. Faigel, Europhys. Lett. **16**, 41 (1991); (b) C.S. Fadley. Mat. Res. Soc. Symp. Proc. **307**, 261 (1993); (c) P.M. Len S. Thevuthasan, C.S. Fadley, A.P. Kaduwela, and M.A. Van Hove, Phys. Rev. B, Rap. Comm. **50**, 11275 (1994).
24. (a) M. Tegze and G. Faigel, Nature **380**, 49 (1996); (b) C.S. Fadley and P.M. Len, Nature **380**, 27 (1996) and unpublished results; (c) T. Gog, P.M. Len, G. Materlik, G. Bahr, C. Sanchez-Hanke, and C.S. Fadley, Phys. Rev. Letters **76**, 3132 (1996); (d) T. Gog, R.-H. Menk, F. Arfelli, P.M. Len, C.S. Fadley, and G. Materlik, Synchrotron Radiation News **9**, 30 (1996); (e) P.M. Len, T. Gog, C.S. Fadley, and G. Materlik, Phys. Rev. B **55**, February, 1997.
25. (a) R.J. Baird, C.S. Fadley, and L.F. Wagner, Phys. Rev. B**15**, 666 (1977); (b) J. Osterwalder, T. Greber, S. Hüfner, and L. Schlapbach, Phys. Rev. B**41**, 12495 (1990); S. Hüfner, J. Osterwalder, T. Greber, and L. Schlapbach, Phys. Rev. B

42, 7350 (1990); G.S. Herman and C.S. Fadley, Phys. Rev. B **43**, 6792 (1991); T. Greber, J. Osterwalder, S. Hüfner, and L. Schlapbach, Phys. Rev. B**44**, 8958 (1991); (c) R. Fasel, P. Aebi, R.G. Agostino, D. Naumovic, J. Osterwalder, A. Santaniello, and L. Schlapbach, Phys. Rev. Letters **76**, 4733 (1996).

26. (a) H.C. Galloway, J.J. Benitez, and M. Salmeron, Surf. Sci. **198**, 127 (1993) and J. Vac. Sci. Technol. A**12**, 2302 (1994); (b) ; Y.J. Kim, Ph. D. thesis, University of Hawaii-Manoa, 1995; Y.J. Kim, C. Westphal, R.X. Ynzunza, Z. Wang, H.C. Galloway, M. Salmeron, M.A. Van Hove, and C.S. Fadley, to be published.
27. (a) C. Günther, J. Vrijmoeth, R.Q. Hwang, and R.J. Behm, Phys. Rev. Lett. **74**, 754 (1995); (b) J.C. Hamilton and S.M. Foiles, Phys. Rev. Lett. **75**, 882 (1995); (c) S.D. Ruebush, R.E. Couch, S. Thevuthasan, Z. Wang, and C.S. Fadley, to be published.
28. (a) D.M. Riffe, G.K. Wertheim, and P.H. Citrin, Phys. Rev. Lett. **53**, 1976 (1989); (b) D. Spanjaard, C. Guillot, M.-C. Desjonquères, G. Treglia, and J. Lecante, Surf. Sci. Repts. **5**, 1 (1985); B. Kim, J. Chen, J.L. Erskine, W.N. Mei, and C.M. Wei, Phys. Rev. B**48**, 4735 (1993).
29. R.X. Ynzunza, F.J. Palomares, E.D. Tober, Z. Wang, H. Daimon, Y. Chen, Z. Hussain, J. Liesegang, M.A. VanHove, and C.S. Fadley. to be published.
30. E. D. Tober, R. X. Ynzunza, F. J. Palomares, Z. Wang, Z. Hussain, M. A. Van Hove, and C. S. Fadley to be published.
31. N.D. Shinn, B. Kim, A.B. Andrews, J.L. Erskine, K.J. Kim, and T.-H. Kang, Mat. Res. Soc. Symp. Proc. **307**, 167 (1993).
32. E.D. Tober, R.X. Ynzunza, C. Westphal, and C.S. Fadley, Phys. Rev. B **53**, 5444 (1996).
33. (a) G. Schönhense, Physica Scripta T**31**, 255 (1990); (b) J. Bansmann, Ch. Ostertag, G. Schönhense, F. Fegel, C. Westphal, M. Getzlaff, F. Schafers, and H. Petersen, Phys. Rev. B**46**, 13496 (1992).
34. (a) V. McKoy and J.A. Stephens, private communication; (b) C. Westphal, A.P. Kaduwela, M.A. Van Hove, and C.S. Fadley, Phys. Rev. B**50**, 6203 (1994).
35. H. Daimon, T. Nakatani, S. Imada, S. Suga, Y. Kagoshima, and T. Miyahara, Jpn. J. Appl. Phys. **32**, L1480 (1993); and H. Daimon, private communication.
36. A.P. Kaduwela, H. Xiao, S. Thevuthasan, M.A. Van Hove, and C.S. Fadley, Phys. Rev. B **52**, 14297 (1995).
37. R.X. Ynzunza, H. Daimon, F.J. Palomares, E.D. Tober, Z. Wang, Z. Hussain, M.A. Van Hove, and C.S. Fadley, to be published.
38. K.E. Johnson, R.J. Wilson, and S. Chiang, Phys. Rev. Lett. **71**, 1055 (1993) and refs. therein.
39. (a) L. Baumgarten, C.M. Schneider, H. Petersen, F. Schafers, and J. Kirschner, Phys. Rev. Lett. **65**, 492 (1990); (b) H. Ebert, L. Baumgarten, C.M. Schneider, and J. Kirschner, Phys. Rev. B44, 4406 (1991); (c) G.D. Waddill, J. Tobin, and D.R. Pappas, Phys. Rev. B**46**, 552 (1992).
40. (a) Ch. Roth, F.U. Hillebrecht, H.B. Rose, and E. Kisker, Phys. Rev. Lett. **70**, 3479 (1993); F. Sirotti and G. Rossi, Phys. Rev. B**49**, 15682 (1994); (b) M. Getzlaff, Ch. Ostertag, G. H. Fecher, N.A. Cherepkov, and G. Schönhense, Phys. Rev. Lett. **73**, 3030 (1994); N.A. Cherepkov, Phys. Rev. B**50**, 13813 (1994); A. Fanelsa, R. Schellenberg, F.U. Hillebrecht, E. Kisker, J.G. Menchero, A.P. Kaduwela, C.S. Fadley, and M.A. Van Hove, Phys. Rev. B **54**, 17962 (1996).
41. J. Morais, R. Denecke, R. X. Ynzunza, J.G. Menchero, J. Liesegang, J. Kortright, Z. Hussain, and C.S. Fadley, to be published.
42. G. van der Laan, E. Arenholz, E. Navas, A. Bauer, and G. Kaindl, Phys. Rev. B53, R5998 (1996).
43. F.U. Hillebrecht, R. Jungblut, and E. Kisker, Phys. Rev. Lett. **65**, 2450 (1990); R. Jungblut, Ch. Roth, F.U. Hillebrecht, and E. Kisker, J. Appl. Phys. **70**, 5923 (1991); R. Jungblut, Ch. Roth, F.U. Hillebrecht, and E. Kisker, Surf. Sci. **269/270**, 615 (1992); T. Kachel, C. Carbone, and W. Gudat, Phys. Rev. B**47**, 15391 (1993); D.G. van Campen, R.J. Pouliot and L.E. Klebanoff, Phys. Rev. B48, 17533 (1993); P.D. Johnson, Y. Liu, Z. Xu, and D.J. Huang, J. Electron Spectrosc. **75**, 245 (1995).
44. F. Zhang, S. Thevuthasan, R.T. Scalettar, R.R.P.Singh, and C.S. Fadley, Phys. Rev. B**51**, 12468 (1995).
45. U. Fano, Phys. Rev. **178**, 131 (1969); U. Heinzmann, J. Kessler, and J. Lorenz,

Phys. Rev. Lett. **25**, 1325 (1970).
46. K. Starke, A.P. Kaduwela, Y. Liu, P.D. Johnson, M.A. Van Hove, C.S. Fadley, V. Chakarian, E.E. Chaban, G. Meigs, and C.T. Chen, Phys. Rev. B **53**, R10544 (1996).
47. J.G. Tobin, C.D. Waddill, D.P. Pappas, E. Tamura, and P. Sterne, J. Vac. Sci. Tech. A**13**, 1574 (1995).
48. N.A. Cherepkov, Phys. Lett. A**40**, 119 (1972) and Adv. At. Mol. Phys. **19**, 395 (1983).
49. (a) E.M.E. Timmermans, G.T. Trammell, and J.P. Hannon, Appl Phys. **73**, 6183 (1993) and Phys. Rev. Lett. **72**, 832 (1994); (b) C.S. Fadley, Mat. Res. Soc. Symp. Proc. **307**, 261 (1993) and Surf. Sci. Rep. **19**, 231 (1993); (c) A.P. Kaduwela, Z. Wang, M.A. Van Hove, and C.S. Fadley, Phys. Rev. B, RC **50**, 9656 (1994); (d) Z.Wang, A.P. Kaduwela, S. Thevuthasan, M.A. Van Hove, and C.S. Fadley, to be published.
50. P.M. Len, E. Rotenberg, J.D. Denlinger, B.P. Tonner, S.D. Kevan, and C.S. Fadley,to be published.
51. W.N. Lipscomb, Acta Crystallographica **2**, 193 (1949); J. Karla and H.A. Hauptmann, Acta Crystallographica **3**, 18 (1950); K. Hümmer and H. Billy, Acta Crystallographica A **38**, 841 (1982); S. L. Chang, Phys. Rev. Letters **48**, 163 (1982).
52. (a) M.J. Bedyzk and G. Materlik, Physical Review B **32**, 6456 (1985); (b) J.T. Hutton, G.T. Trammell, and J.P. Hannon, Phys. Rev. B **31**, 420 (1985), and Phy. Rev.B **31**, 743 (1985).
53. S. M. Goldberg, R. J. Baird, S. Kono, N. F. T. Hall, and C. S. Fadley, J. Electron Spectrosc. **21**, 1 (1980); R. Trehan, C. S. Fadley and J. Osterwalder, J. Electron Spectrosc. **42**, 187 (1987).